



ATLAS
EXPERIMENT



Searches for Higgs boson pair production with the full LHC Run 2 dataset in ATLAS

James Grundy
The University of Oxford

*10th International Conference on
New Frontiers in Physics (ICNFP 2021)*
24/08/21

Theoretical Motivation

Why study Higgs pair production?

Theoretical Motivation

Why study Higgs pair production?

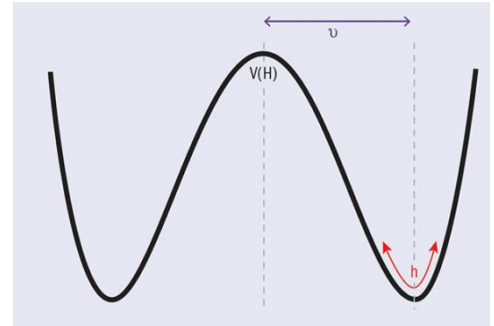
$$\begin{aligned}\mathcal{L} = & -\frac{1}{4} F_{\mu\nu} F^{\mu\nu} \\ & + i \bar{\Psi} \not{D} \Psi + \text{h.c.} \\ & + \bar{\Psi}_i y_{ij} \Psi_j \phi + \text{h.c.} \\ & + |D_\mu \phi|^2 - V(\phi)\end{aligned}$$

Theoretical Motivation

Why study Higgs pair production?

$$\begin{aligned}\mathcal{L} = & -\frac{1}{4} F_{\mu\nu} F^{\mu\nu} \\ & + i\bar{\Psi}\not{D}\Psi + h.c. \\ & + \bar{\Psi}_i y_{ij} \Psi_j \phi + h.c. \\ & + \frac{1}{2} D_\mu \phi^2 - \underbrace{V(\phi)}\end{aligned}$$

$$V(\phi) = -\mu^2|\phi|^2 + \lambda|\phi|^4$$

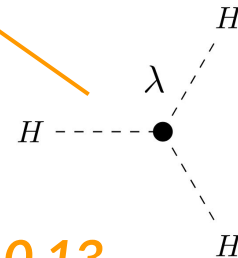
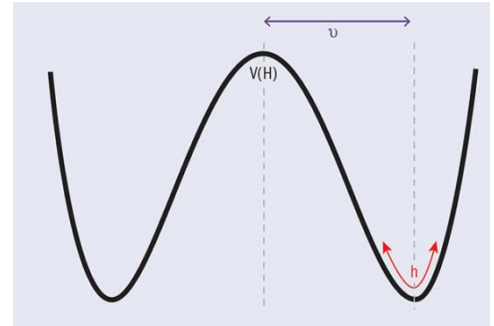


Theoretical Motivation

Why study Higgs pair production?

$$\begin{aligned} \mathcal{L} = & -\frac{1}{4} F_{\mu\nu} F^{\mu\nu} \\ & + i \bar{\Psi} \not{D} \Psi + h.c. \\ & + \bar{\Psi}_i y_{ij} \Psi_j \phi + h.c. \\ & + \frac{1}{2} \partial_\mu \phi^2 - \underbrace{V(\phi)} \end{aligned}$$

$$V(\phi) = -\mu^2 |\phi|^2 + \lambda |\phi|^4$$



*Trilinear Higgs
Self-Coupling*

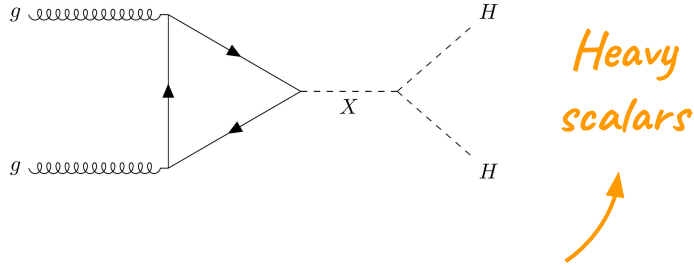
SM $\lambda \sim 0.13$

Beyond the Standard Model Effects

Beyond the Standard Model Effects

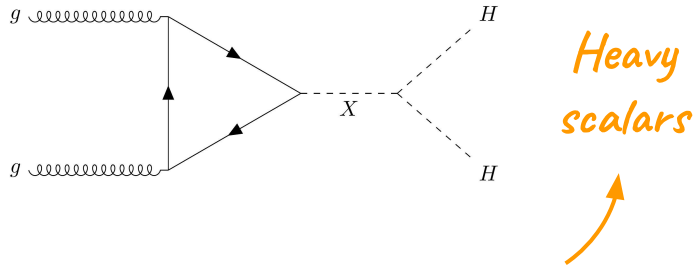
**BSM resonances predicted
to decay to HH...**

Beyond the Standard Model Effects



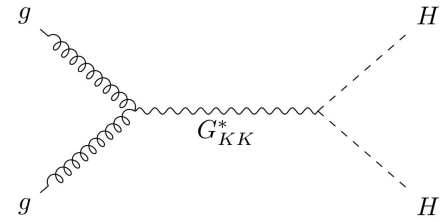
**BSM resonances predicted
to decay to HH...**

Beyond the Standard Model Effects



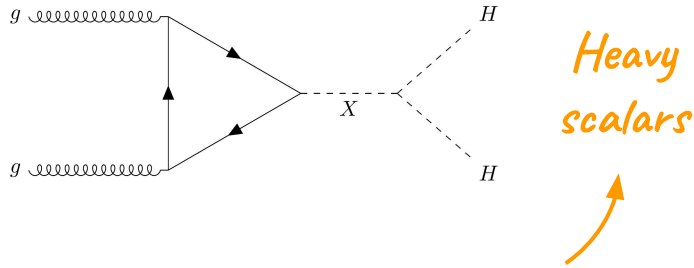
BSM resonances predicted to decay to HH...

Kaluza-Klein Gravitons



Several others...

Beyond the Standard Model Effects



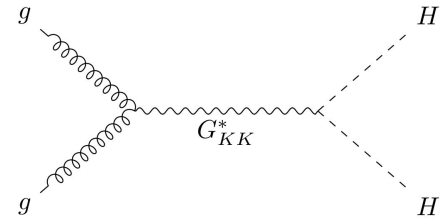
Heavy scalars



BSM resonances predicted to decay to HH...

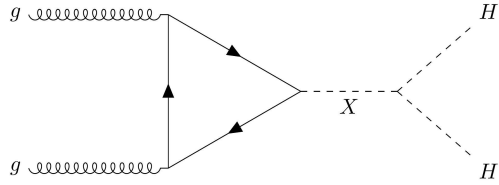
BSM physics that can alter non-resonant HH production...

Kaluza-Klein Gravitons



Several others...

Beyond the Standard Model Effects



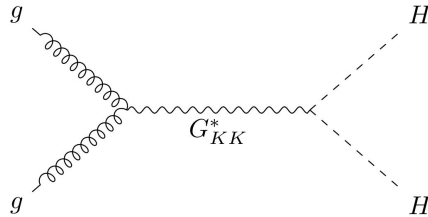
Heavy scalars

Modifications to the Higgs self-coupling

BSM physics that can alter non-resonant HH production...

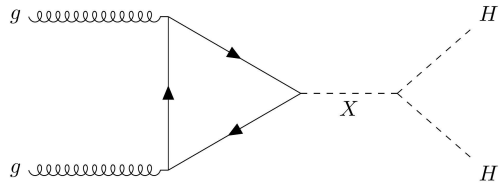
BSM resonances predicted to decay to HH...

Kaluza-Klein Gravitons



Several others...

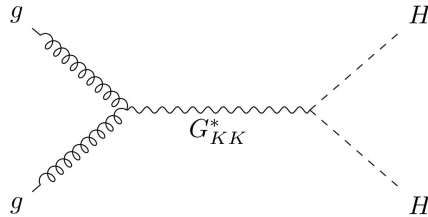
Beyond the Standard Model Effects



Heavy scalars

BSM resonances predicted to decay to HH...

Kaluza-Klein Gravitons



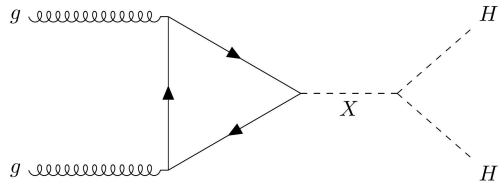
Several others...

Modifications to the Higgs self-coupling

New couplings of Higgs to SM particles

BSM physics that can alter non-resonant HH production...

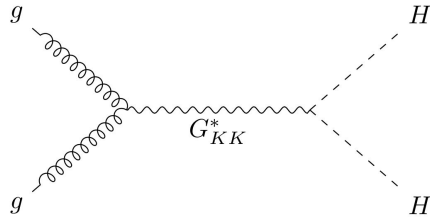
Beyond the Standard Model Effects



Heavy scalars

BSM resonances predicted to decay to HH...

Kaluza-Klein Gravitons



Several others...

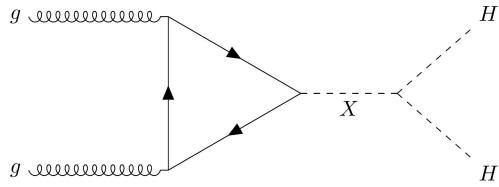
Modifications to the Higgs self-coupling

New couplings of Higgs to SM particles

BSM physics that can alter non-resonant HH production...

New particles contributing in loops

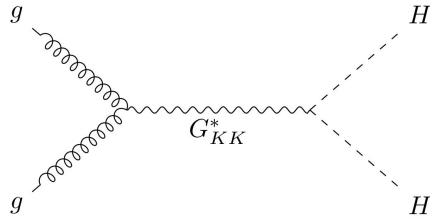
Beyond the Standard Model Effects



Heavy scalars

BSM resonances predicted to decay to HH...

Kaluza-Klein Gravitons



Several others...

Modifications to the Higgs self-coupling

New couplings of Higgs to SM particles

BSM physics that can alter non-resonant HH production...

New particles contributing in loops

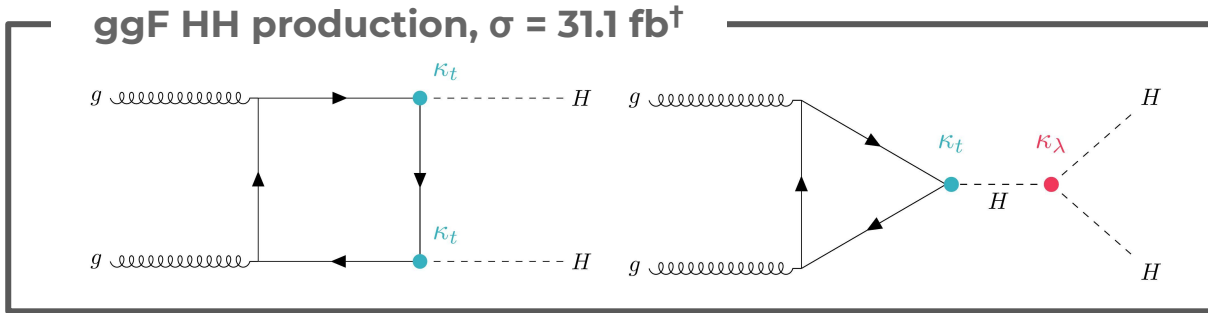
Rich theoretical basis to search for BSM effects in the HH production!

So far, no such BSM effects have been observed experimentally.

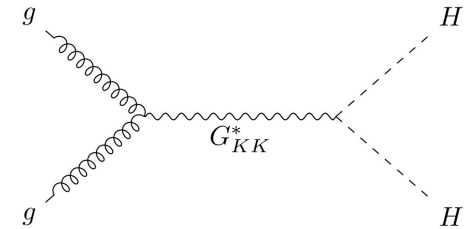
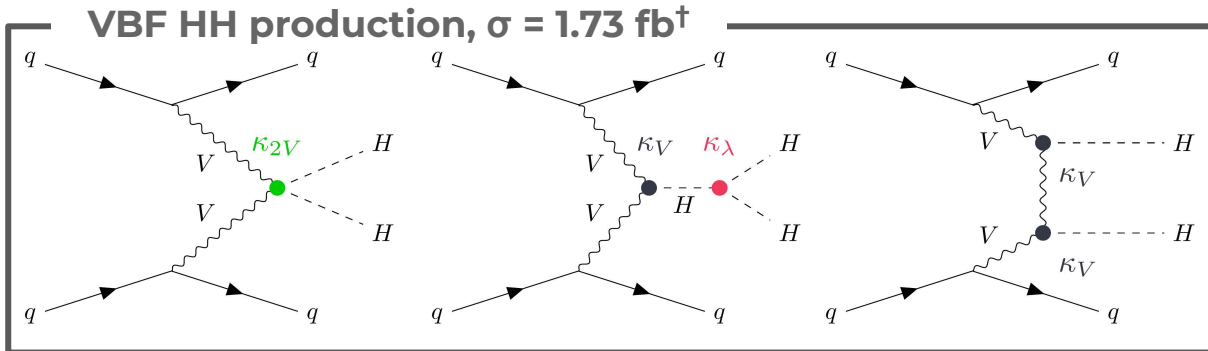
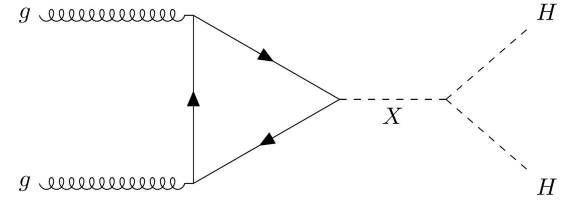
HH Production at the LHC

Total HH production $\sigma = 34.4 \text{ fb}^\dagger$, which is ~ 1000 times smaller than σ_H !

$$\kappa = c/c^{SM}$$



Resonant ggF HH production



...

ATLAS HH Analyses

HH analyses in ATLAS focus primarily on setting limits on σ_{HH} , couplings involving HH and BSM resonance models.

There are several HH analyses targeting different decay channels \rightarrow overall aim: combine results to maximise sensitivity.

Today, will cover the latest results from:

- [HH \$\rightarrow\$ bbyy](#)
- [HH \$\rightarrow\$ bb \$\tau\tau\$](#)
- [HH \$\rightarrow\$ bbbb](#)


All use the full ATLAS Run 2 (2015-18) dataset ($\mathcal{L} = 139 \text{ fb}^{-1}$) at $\sqrt{s} = 13 \text{ TeV}$.

HH decay branching ratios

$b\bar{b}$	W^+W^-	gg	$\tau^+\tau^-$	$c\bar{c}$	ZZ	$\gamma\gamma$	Z γ	$\mu^+\mu^-$	
33.9%	24.9%	9.5%	7.3%	3.4%	3.1%	0.3%	0.2%	< 0.1%	$b\bar{b}$
	4.6%	3.5%	2.7%	1.2%	1.1%	< 0.1%	< 0.1%	< 0.1%	W^+W^-
		0.7%	1.0%	0.5%	0.4%	< 0.1%	< 0.1%	< 0.1%	gg
			0.4%	0.4%	0.3%	< 0.1%	< 0.1%	< 0.1%	$\tau^+\tau^-$
				< 0.1%	0.2%	< 0.1%	< 0.1%	< 0.1%	$c\bar{c}$
					< 0.1%	< 0.1%	< 0.1%	< 0.1%	ZZ
						< 0.1%	< 0.1%	< 0.1%	$\gamma\gamma$
							< 0.1%	< 0.1%	Z γ
								< 0.1%	$\mu^+\mu^-$

Data from LHCHSWG (CERN YR 4)

HH \rightarrow bb $\gamma\gamma$

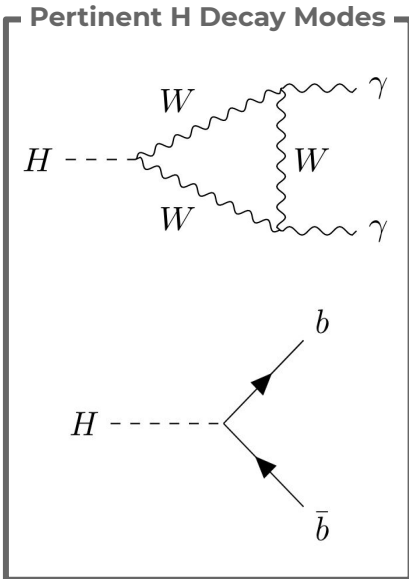


Analysis Overview

Non-resonant: search for HH production for κ_λ hypotheses in range -10 to 10 (SM = 1).

Resonant: search for a narrow-width scalar resonance with mass between 251-1000 GeV.

Low HH BR at $\sim 0.3\%$, but clean signal due to $H \rightarrow \gamma\gamma$.

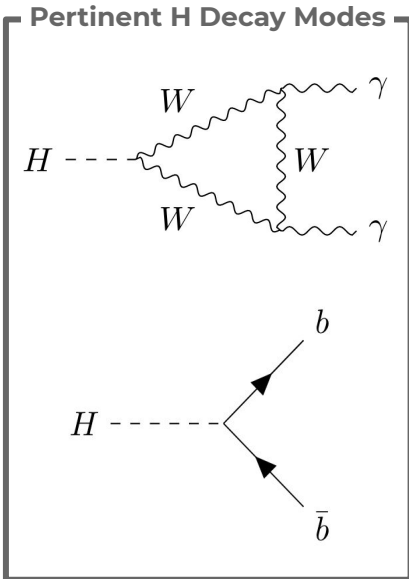


Analysis Overview

Non-resonant: search for HH production for κ_λ hypotheses in range -10 to 10 (SM = 1).

Resonant: search for a narrow-width scalar resonance with mass between 251-1000 GeV.

Low HH BR at $\sim 0.3\%$, but clean signal due to $H \rightarrow \gamma\gamma$.



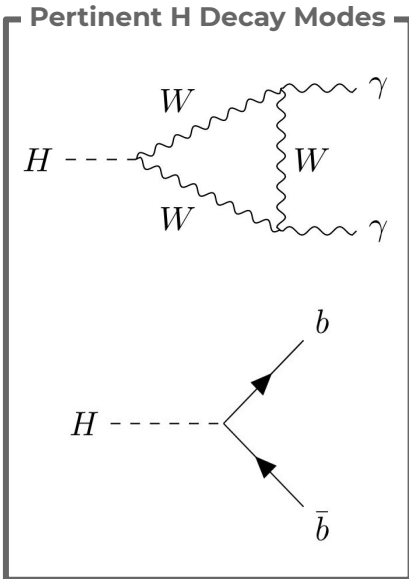
*di-photon
triggers*

Analysis Overview

Non-resonant: search for HH production for κ_λ hypotheses in range -10 to 10 (SM = 1).

Resonant: search for a narrow-width scalar resonance with mass between 251-1000 GeV.

Low HH BR at $\sim 0.3\%$, but clean signal due to $H \rightarrow \gamma\gamma$.



*di-photon
triggers*

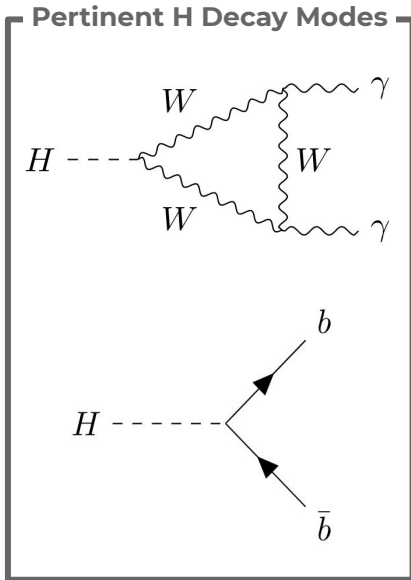
*Selected
events with 2
photons and 2
b-tagged jets*

Analysis Overview

Non-resonant: search for HH production for κ_λ hypotheses in range -10 to 10 (SM = 1).

Resonant: search for a narrow-width scalar resonance with mass between 251-1000 GeV.

Low HH BR at ~0.3%, but clean signal due to $H \rightarrow \gamma\gamma$.



*di-photon
triggers*

*Use MVA to
separate
HH sig from
bkg*

*Selected
events with 2
photons and 2
b-tagged jets*

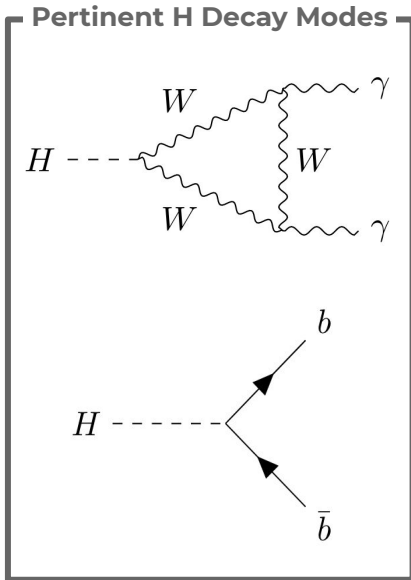
*Main bkg is $\gamma\gamma$ +jets, with
some $t\bar{t}\gamma\gamma$, fakes and single H*

Analysis Overview

Non-resonant: search for HH production for κ_λ hypotheses in range -10 to 10 (SM = 1).

Resonant: search for a narrow-width scalar resonance with mass between 251-1000 GeV.

Low HH BR at $\sim 0.3\%$, but clean signal due to $H \rightarrow \gamma\gamma$.



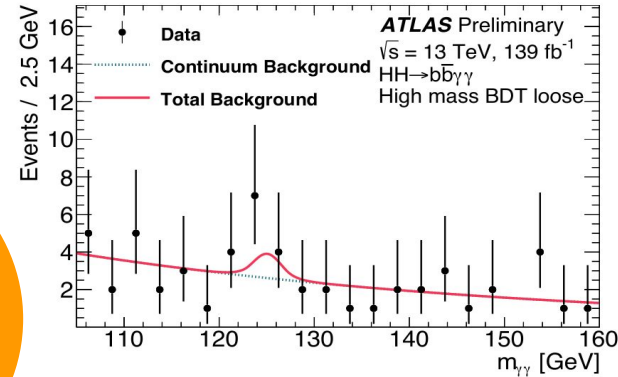
di-photon
triggers

Use MVA to
separate
HH sig from
bkg

Selected
events with 2
photons and 2
 b -tagged jets

Model sig/bkg
with functions
fit to data to
test
hypotheses!

Main bkg is $\gamma\gamma$ +jets, with
some $t\bar{t}\gamma\gamma$, fakes and single H

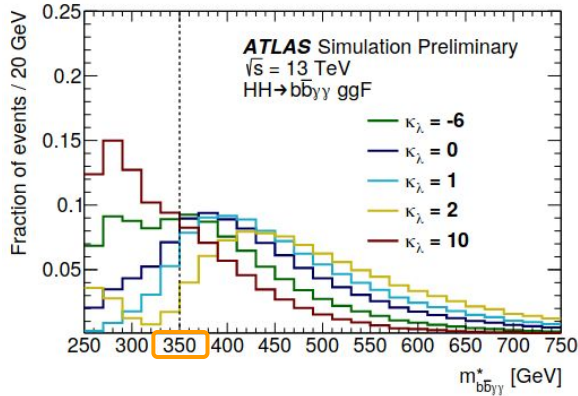


Dominant analysis
uncertainty is statistical!

Details of Non-Resonant Analysis

Details of Non-Resonant Analysis

Categorisation defined based on HH mass

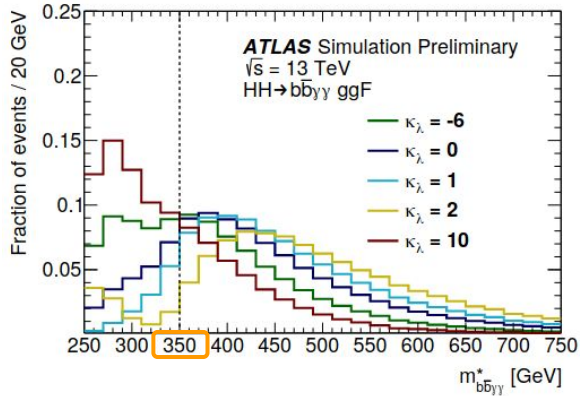


Low mass category

High mass category

Details of Non-Resonant Analysis

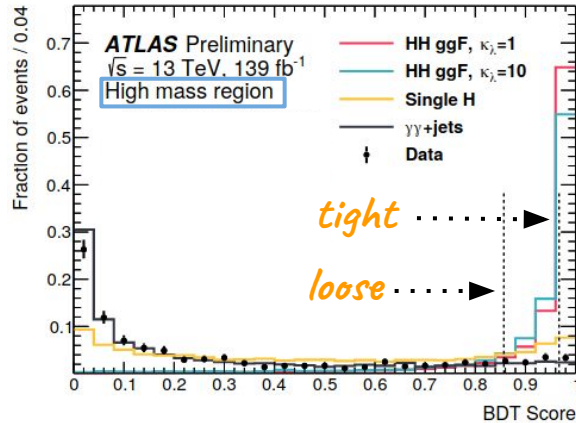
Categorisation defined based on HH mass



Low mass category

High mass category

A BDT is trained in each mass category to separate sig and bkg.



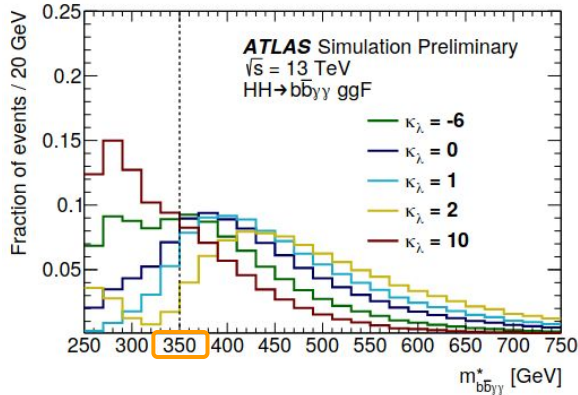
tight

loose

Extra categorisation defined based on BDT score: "loose" and "tight"

Details of Non-Resonant Analysis

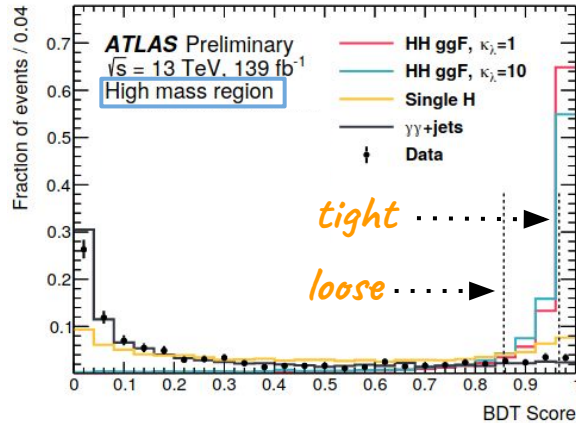
Categorisation defined based on HH mass



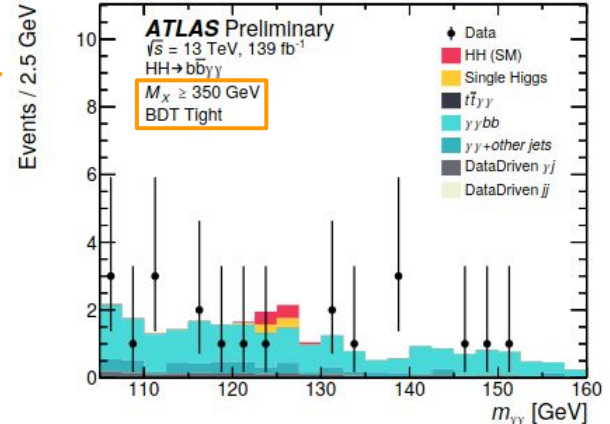
Low mass category

High mass category

A BDT is trained in each mass category to separate sig and bkg.



Extra categorisation defined based on BDT score: "loose" and "tight"



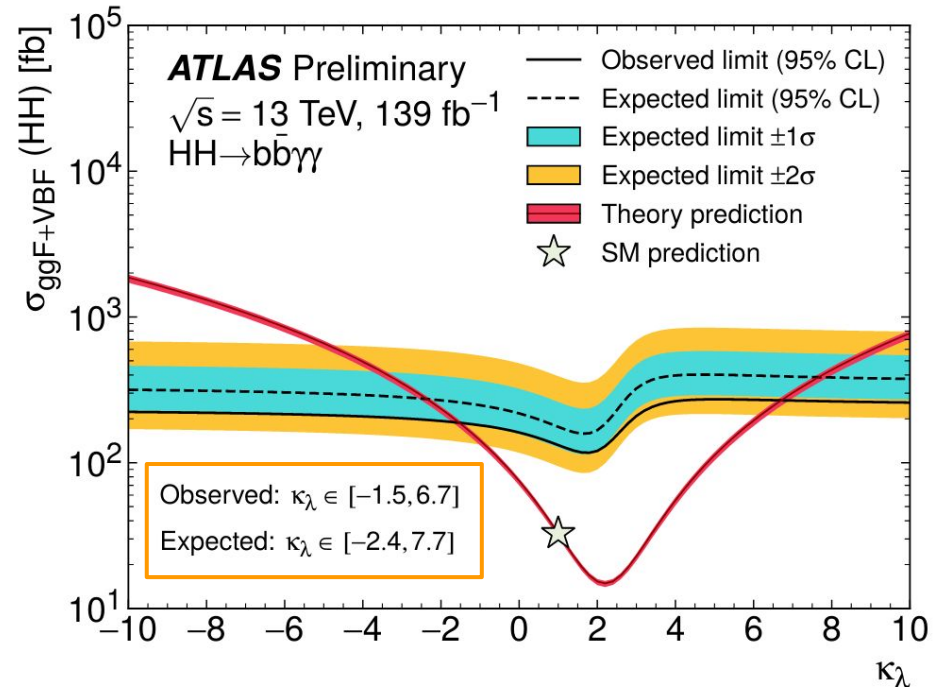
Four categories: low/high mass x loose/tight BDT score.

Non-Resonant Results

No significant excesses over background observed \rightarrow set limits¹ on σ_{HH} and κ_λ .

$$\mu = \sigma / \sigma_{SM}$$

	Limit on σ_{HH} [fb]	Limit on μ
Obs' (Exp')	130 (180)	4.1 (5.5)



Non-Resonant Results

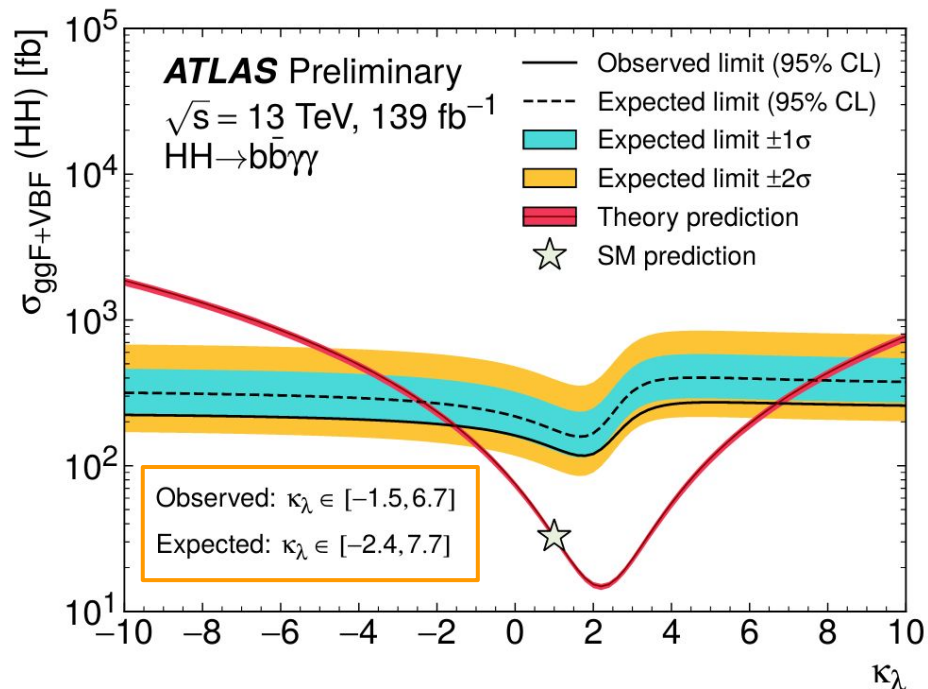
No significant excesses over background observed \rightarrow set limits¹ on σ_{HH} and κ_λ .

$$\mu = \sigma / \sigma_{SM}$$

	Limit on σ_{HH} [fb]	Limit on μ
Obs' (Exp')	130 (180)	4.1 (5.5)

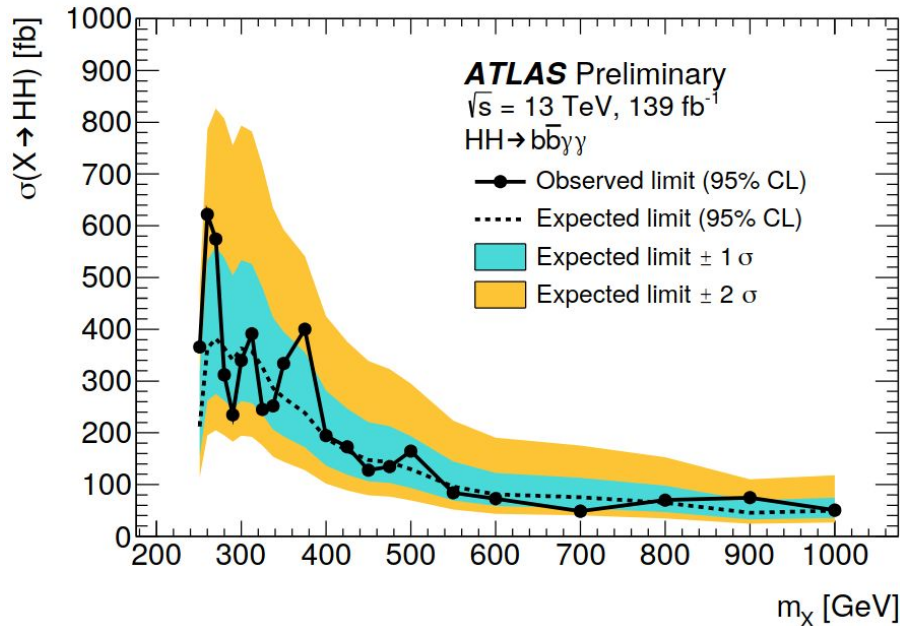
5-fold improvement on previous analysis²!

~3-fold due to analysis improvements
e.g. $m_{b\bar{b}\gamma\gamma}^*$ categories, MVA event selection,
improved object reco/calibration.



Resonant Results

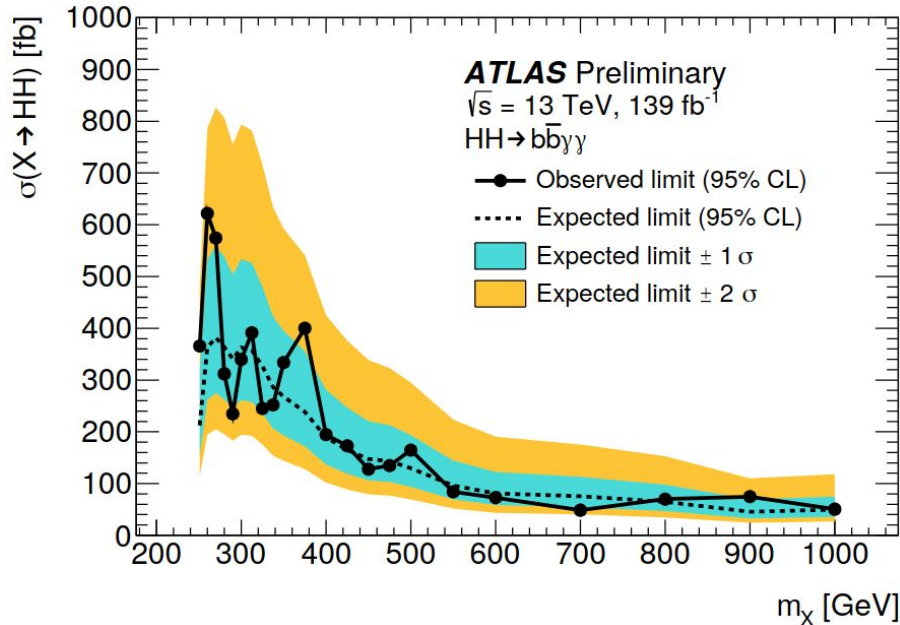
No significant excesses over background observed \rightarrow set upper limits¹ on σ for narrow width scalar resonances at the various mass hypotheses tested.



For $251 \leq m_x \leq 1000 \text{ GeV}$, obs' (exp')
varies between 610–47 fb (360–43 fb)

Resonant Results

No significant excesses over background observed \rightarrow set upper limits¹ on σ for narrow width scalar resonances at the various mass hypotheses tested.




For $251 \leq m_{\text{X}} \leq 1000 \text{ GeV}$, obs' (exp')
varies between 610–47 fb (360–43 fb)

*2 to 3-fold improvement on previous
analysis² depending on m_{X}*

~1/3 due to analysis improvements!

$HH \rightarrow bb\tau\tau$

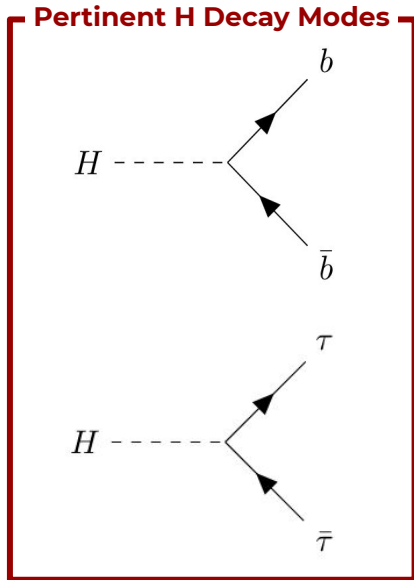


Analysis Overview

Non-resonant: search for SM non-resonant HH production.

Resonant: search for a narrow-width scalar resonance with mass in range 251 to 1600 GeV.

Balance of moderate HH BR of ~7.3% and relatively clean $\tau\tau$ signature.

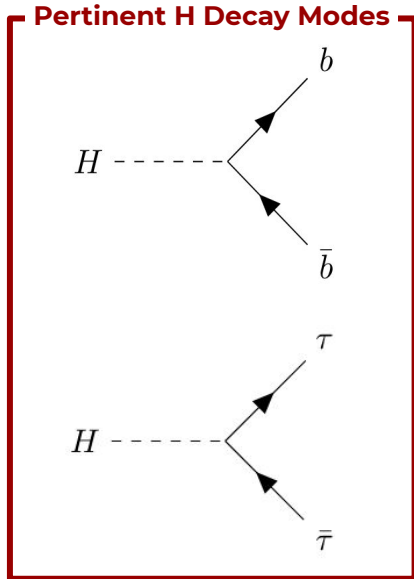


Analysis Overview

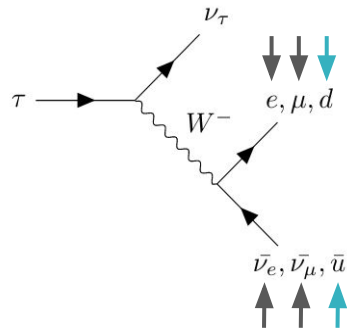
Non-resonant: search for SM non-resonant HH production.

Resonant: search for a narrow-width scalar resonance with mass in range 251 to 1600 GeV.

Balance of moderate HH BR of $\sim 7.3\%$ and relatively clean $\tau\tau$ signature.



*τ s can decay
hadronically or
leptonically...*

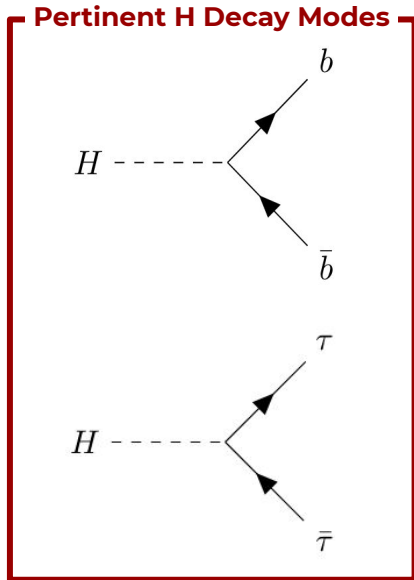


Analysis Overview

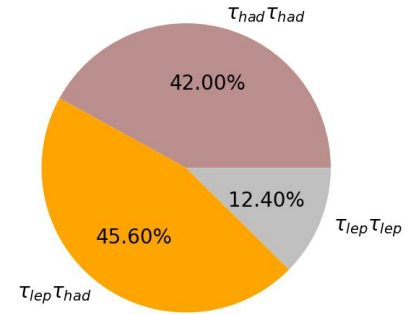
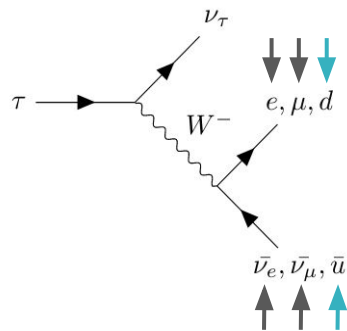
Non-resonant: search for SM non-resonant HH production.

Resonant: search for a narrow-width scalar resonance with mass in range 251 to 1600 GeV.

Balance of moderate HH BR of $\sim 7.3\%$ and relatively clean $\tau\tau$ signature.



τ s can decay
hadronically or
leptonically...



Further split $\tau_{lep} \tau_{had}$ SR:
Single Lepton Trigger (SLT)
Lepton Tau Trigger (LTT)

Three signal regions in total!

Analysis Overview

Main background is top,

(Z+jets and multijet.

*Modelled true τ
bkg using MC.*

*Modelled fake
contribution
using data.*

Analysis Overview

Main background is top,

(Z+jets and multijet.

Modelled true τ
bkg using MC.
Modelled fake
contribution
using data.

Used suite of
MVAs to
separate sig
from bkg

	Resonant	Non-Resonant	
		$T_{had} T_{had}$	$T_{lep} T_{had}$
MVA	Parameterised NN (m_x)	BDT	NN

Analysis Overview

Main background is top,
(Z+jets and multijet.

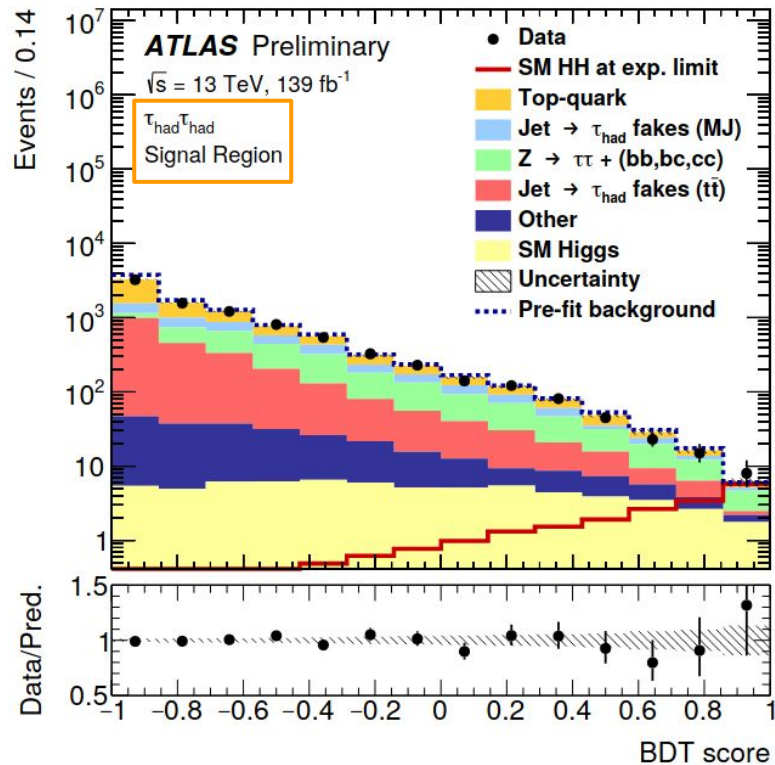
Modelled true τ
bkg using MC.
Modelled fake
contribution
using data.

Used suite of
MVAs to
separate sig
from bkg

Variable of
interest is MVA
score

Fit templates
to data to
test
hypotheses!

	Resonant	Non-Resonant	
		$\tau_{had}\tau_{had}$	$\tau_{lep}\tau_{had}$
MVA	Parameterised NN (m_x)	BDT	NN



Non-Resonant Results

No significant excesses over background observed \rightarrow set upper limits¹ on σ_{HH} .

Obs' (Exp')	Limit on σ_{HH} [fb]	Limit on μ
$T_{had}T_{had}$	145 (131)	4.9 (4.5)
$T_{lep}T_{had}$	265 (231)	9.0 (7.9)
Combined	135 (114)	4.7 (3.9)

Non-Resonant Results

No significant excesses over background observed \rightarrow set upper limits¹ on σ_{HH} .

Obs' (Exp')	Limit on σ_{HH} [fb]	Limit on μ
$T_{had}T_{had}$	145 (131)	4.9 (4.5)
$T_{lep}T_{had}$	265 (231)	9.0 (7.9)
Combined	135 (114)	4.7 (3.9)

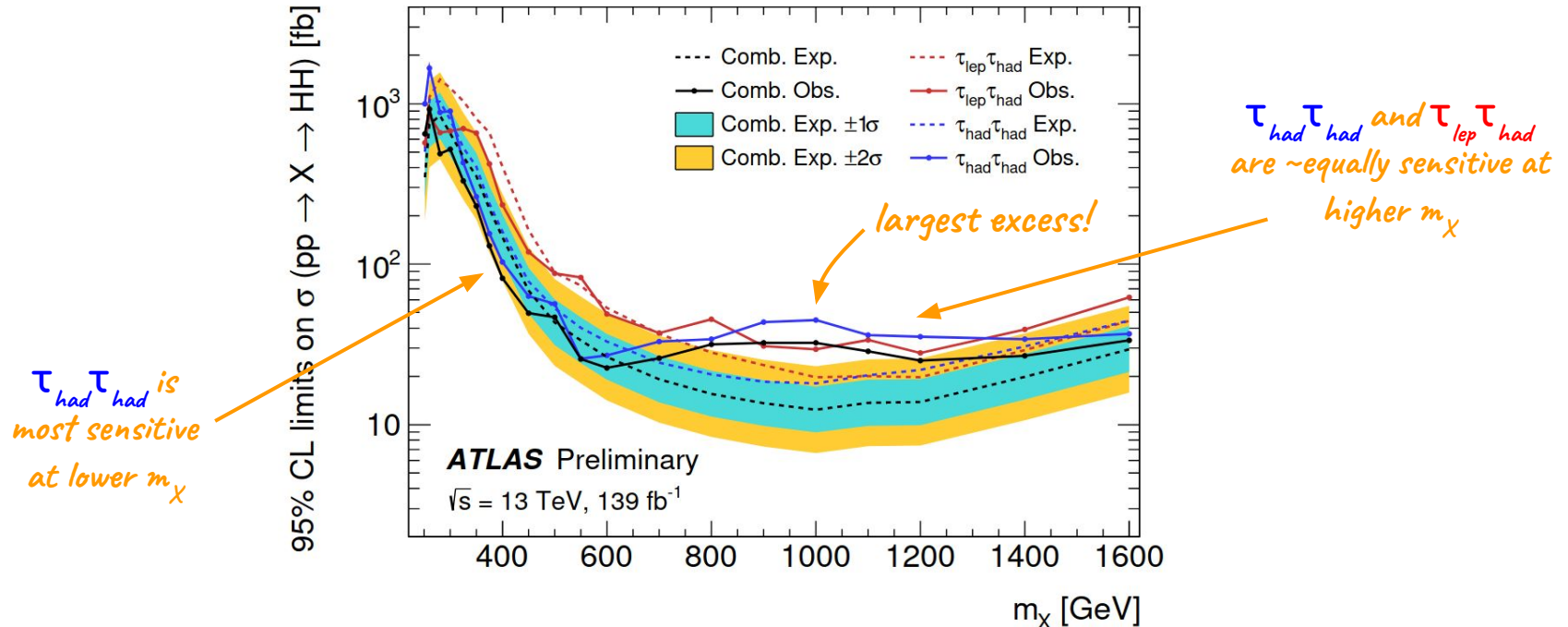
4-fold improvement on previous SM limits².

*~2-fold due to analysis improvements
e.g. MVA event selection, improved fake
estimate, object reco/calibration.*

*Dominant uncertainty is statistical.
Largest systematic is background modelling.*

Resonant Results

At $m_X = 1$ TeV, a small excess of local significance 3.0σ and a global significance $2.0 (+0.4, -0.2)\sigma$ was observed.



HH \rightarrow bbbb

Analysis Overview

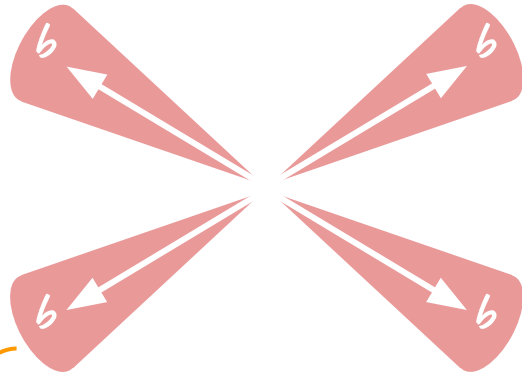
Resonant: search for narrow-width scalar resonance and spin-2 Kaluza-Klein Graviton[†] resonance with mass in range 251-3000 GeV.

Largest HH BR (~34%) but dominant multijet background → data-driven background estimate.

Two categories:

Resolved

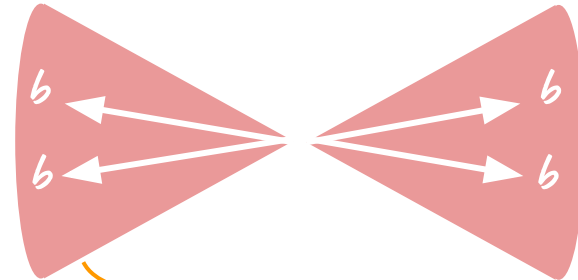
Mass range: 251-1500 GeV



Reconstruct small radius jets

Boosted

Mass range: 900-3000 GeV

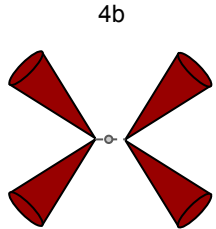


Reconstruct large radius jets

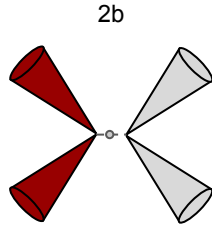
Resolved Analysis Overview

Fully
data-driven
bkg model

Build 4b bkg
from 2b



Small-R
non-b-tagged
PFlow jet



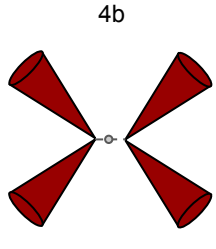
Small-R
b-tagged
PFlow jet



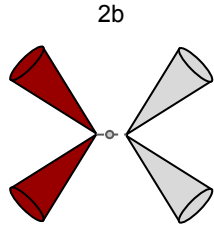
Resolved Analysis Overview

Fully data-driven bkg model

Build 4b bkg from 2b



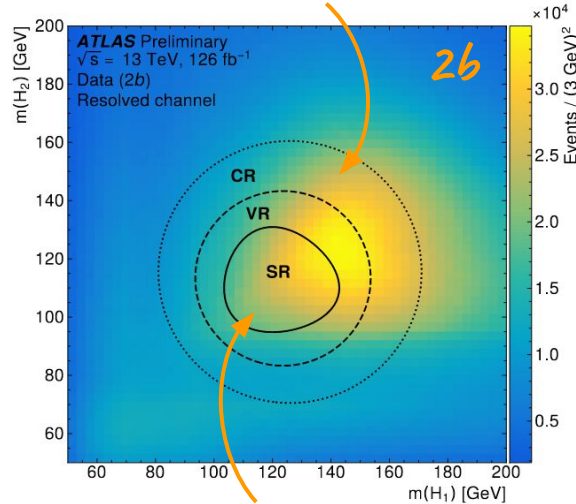
Small-R non-b-tagged PFlow jet



Small-R b-tagged PFlow jet



Derive weights in CR by mapping to 2b to 4b

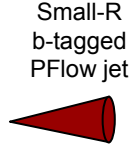
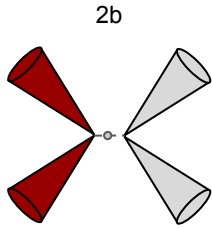
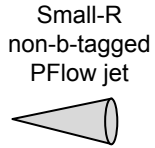
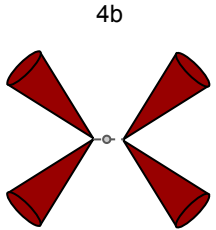


Apply weights to 2b SR to get background estimate!

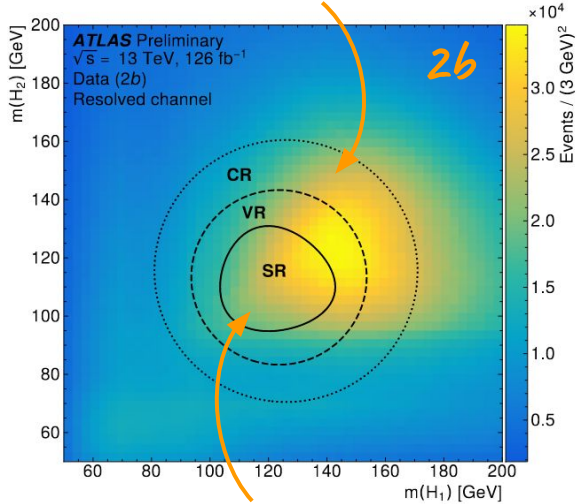
Resolved Analysis Overview

Fully data-driven bkg model

Build 4b bkg from 2b

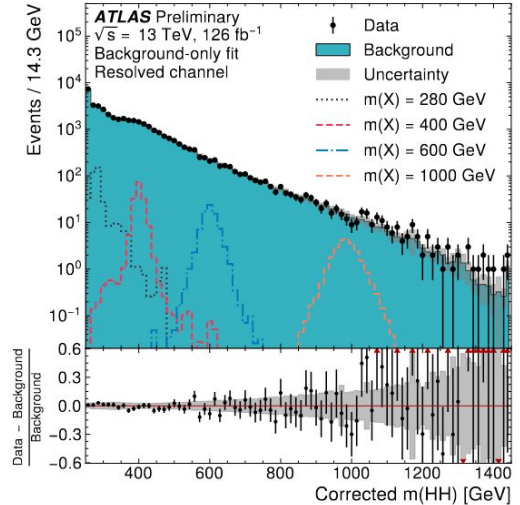


Derive weights in CR by mapping to 2b to 4b



Apply weights to 2b SR to get background estimate!

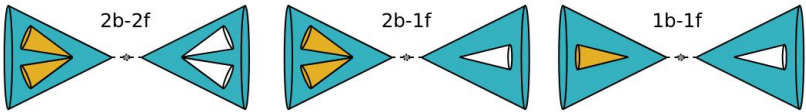
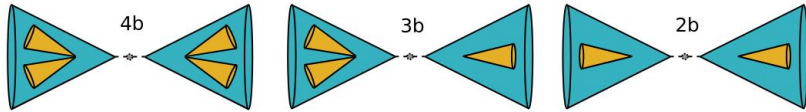
Fit templates to data to test hypotheses!



Boosted Analysis Overview

Categorise based on the no. of track jets and their tag

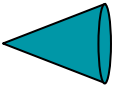
*Build 4b bkg from 2b2f,
3b from 2b1f,
2b from 1b1f!*



Large-R PFlow jet

b-tagged track jet

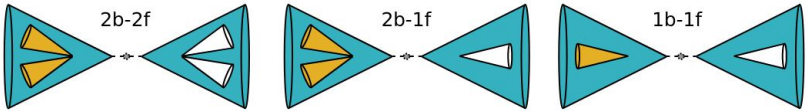
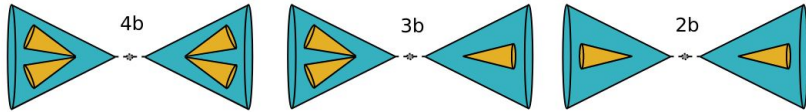
non-b-tagged track jet



Boosted Analysis Overview

Categorise based on the no. of track jets and their tag

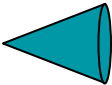
Build 4b bkg from 2b2f,
3b from 2b1f,
2b from 1b1f!



Large-R PFlow jet

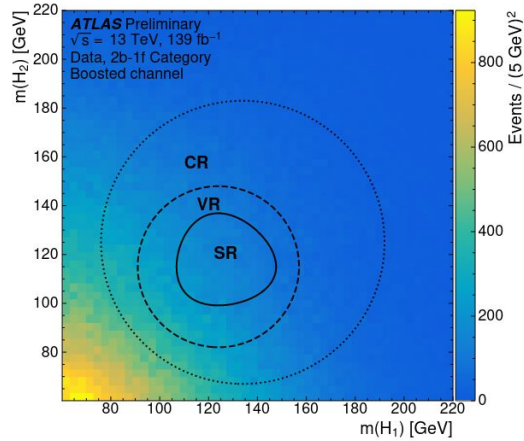
b-tagged track jet

non-b-tagged track jet



James Grundy

Region definitions slightly different from Resolved



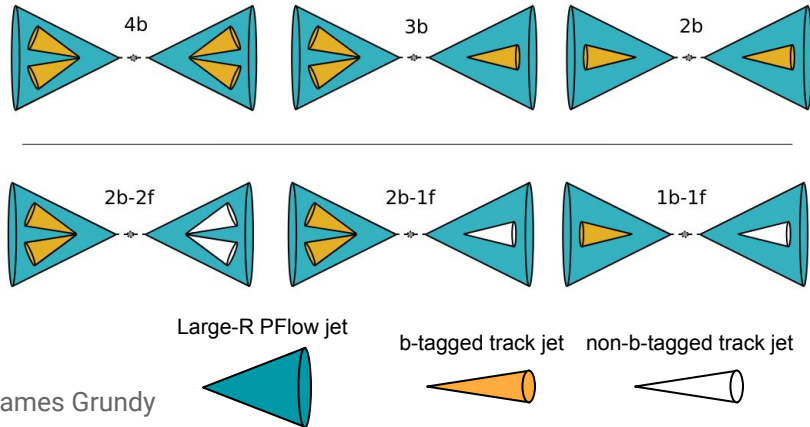
Up to 30% tt .
 multijet:
 data-driven
 tt : MC

24/08/21

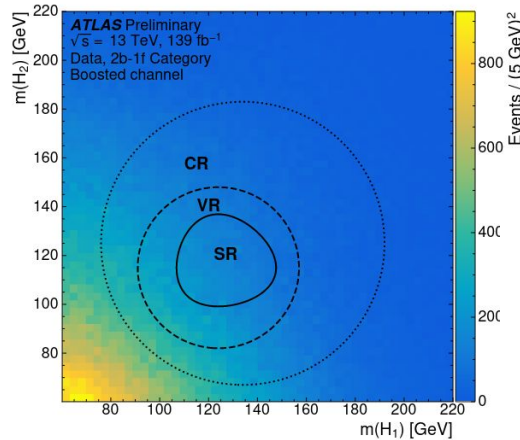
Boosted Analysis Overview

Categorise based on the no. of track jets and their tag

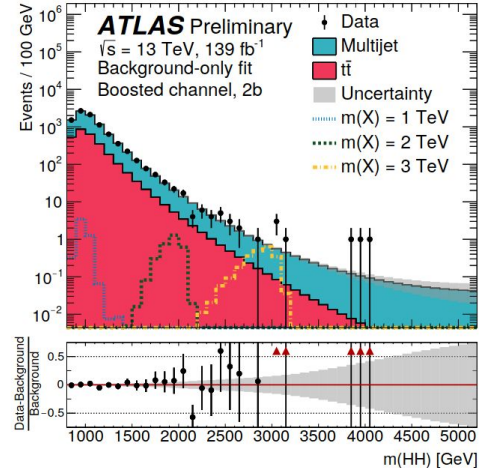
Build 4b bkg from 2b2f,
3b from 2b1f,
2b from 1b1f!



Region definitions slightly different from Resolved



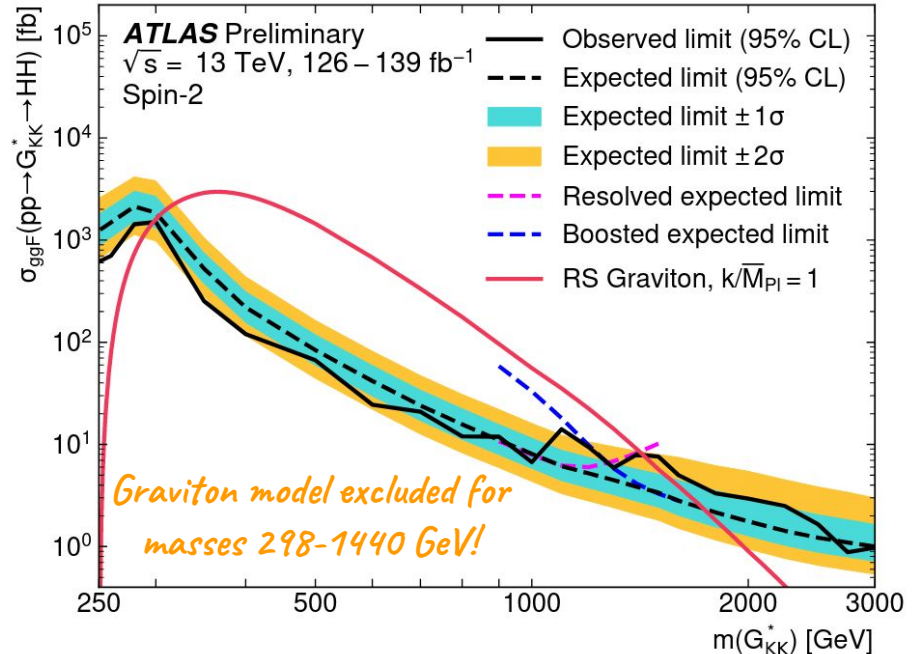
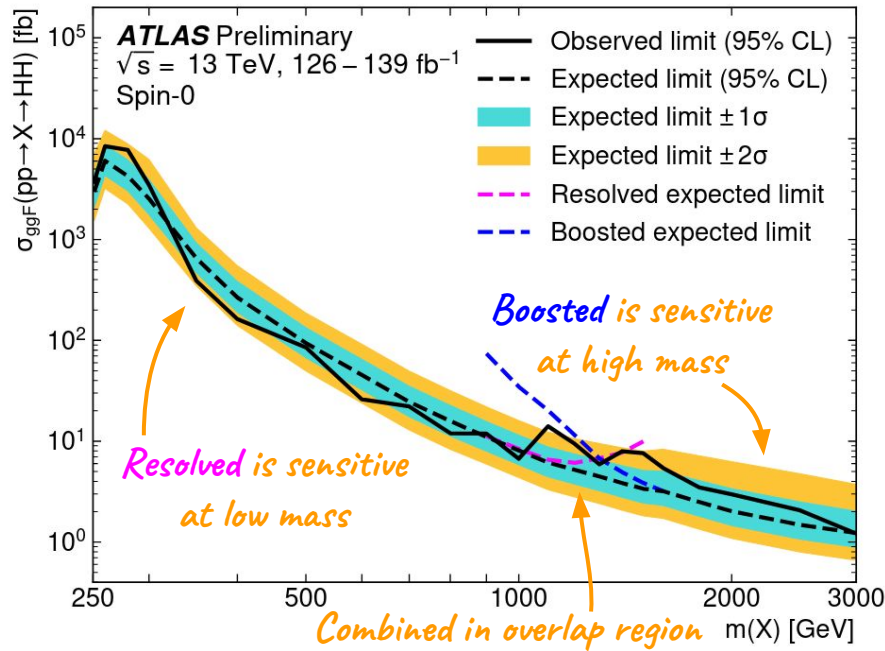
Fit templates to data to test hypotheses!



Up to 30% $t\bar{t}$.
multijet:
data-driven
 $t\bar{t}$: MC

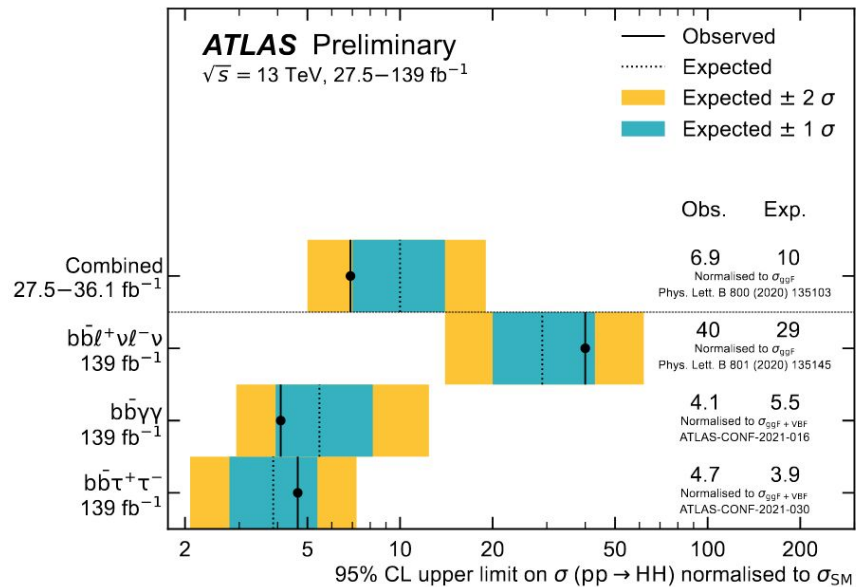
HH \rightarrow bbbb Results

No significant excesses above background observed \rightarrow set upper limits[†] on σ for two models at various mass hypotheses.



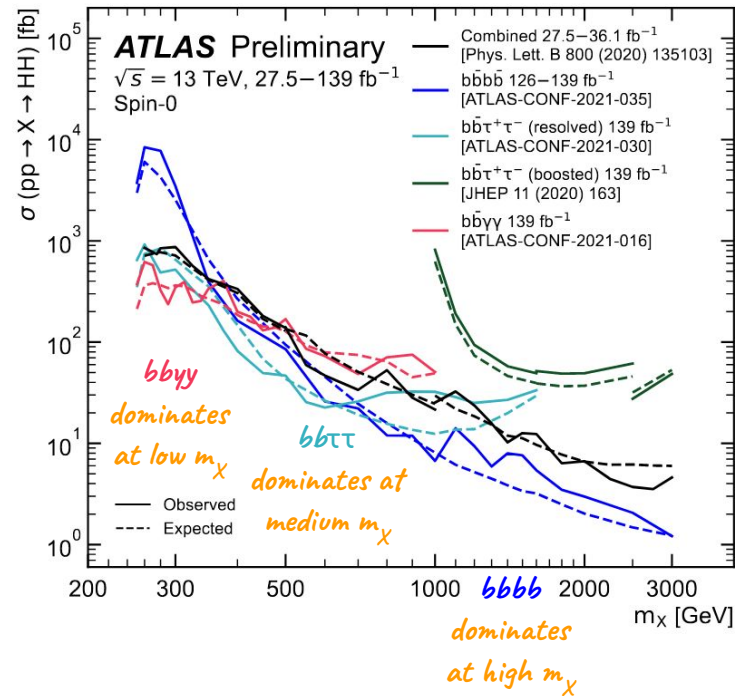
Results Summary

Non-Resonant SM HH production



*Individual channels showing improvement over
36fb⁻¹ combination!*

Scalar resonance



Looking Forward...

~21 x as much as full Run 2 dataset!

Projections for High Luminosity LHC (HL-LHC) with 3ab^{-1} of data based on 36fb^{-1} HH analyses (not those shown today!):

Channel	Statistical-only	Statistical + Systematic
$HH \rightarrow b\bar{b}b\bar{b}$	1.2	0.5
$HH \rightarrow b\bar{b}\tau^+\tau^-$	2.3	2.0
$HH \rightarrow b\bar{b}\gamma\gamma$	2.1	2.0
Combined	3.3σ	2.9σ

Looking Forward...

~21 x as much as full Run 2 dataset!

Projections for High Luminosity LHC (HL-LHC) with 3ab^{-1} of data based on 36fb^{-1} of HH analyses (not those shown today!):

Channel	Statistical-only	Statistical + Systematic
$HH \rightarrow b\bar{b}b\bar{b}$	1.2	0.5
$HH \rightarrow b\bar{b}\tau^+\tau^-$	2.3	2.0
$HH \rightarrow b\bar{b}\gamma\gamma$	2.1	2.0
Combined	3.3σ	2.9σ

Future is bright for HH searches in ATLAS in the near future and beyond!

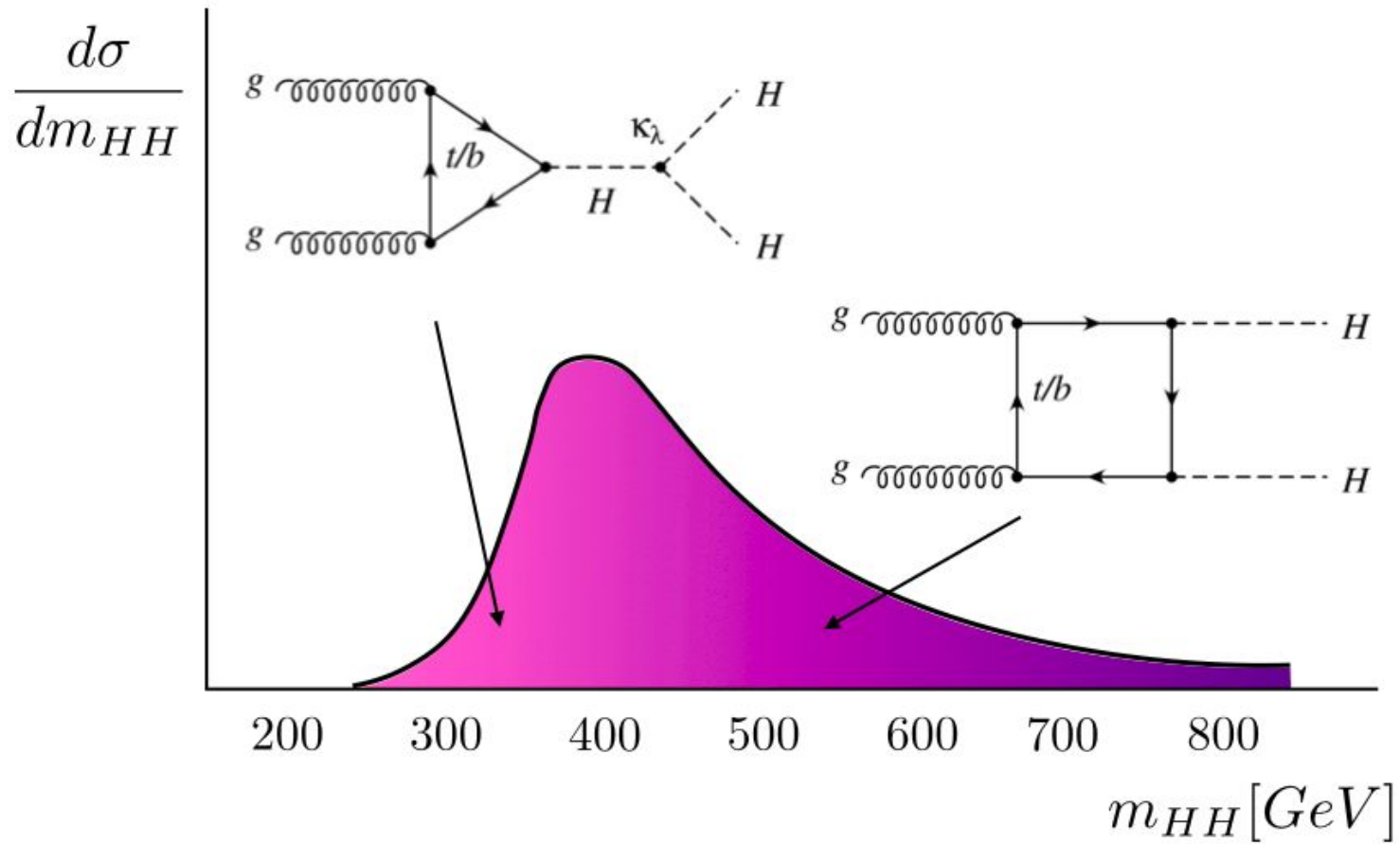
Back Up Slides



Title

Primary text

Side note



HH → bbγγ



$$m_{b\bar{b}\gamma\gamma}^* = m_{b\bar{b}\gamma\gamma} - m_{b\bar{b}} - m_{\gamma\gamma} + 250 \text{ GeV}$$

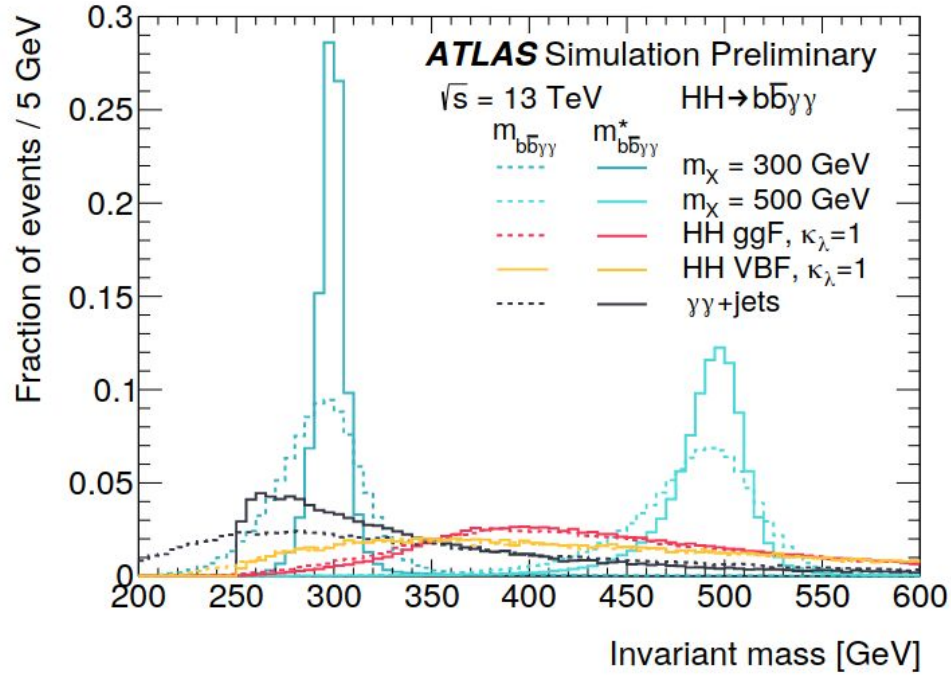
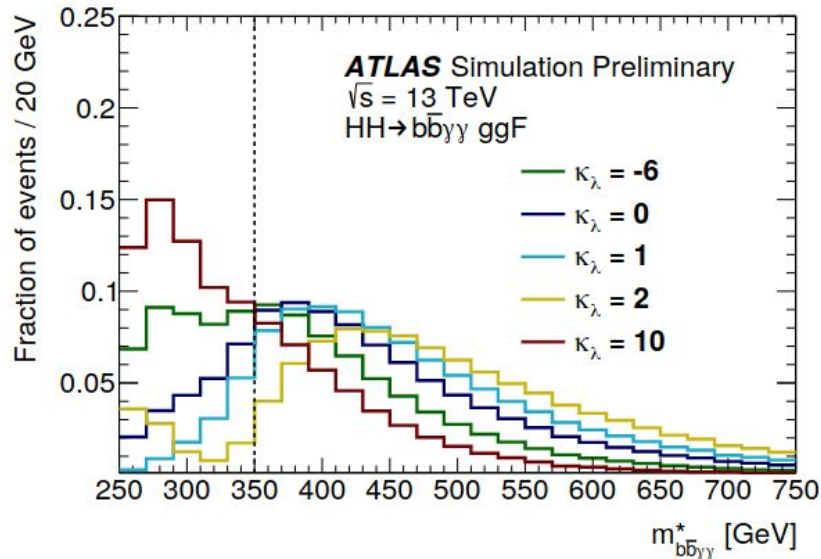
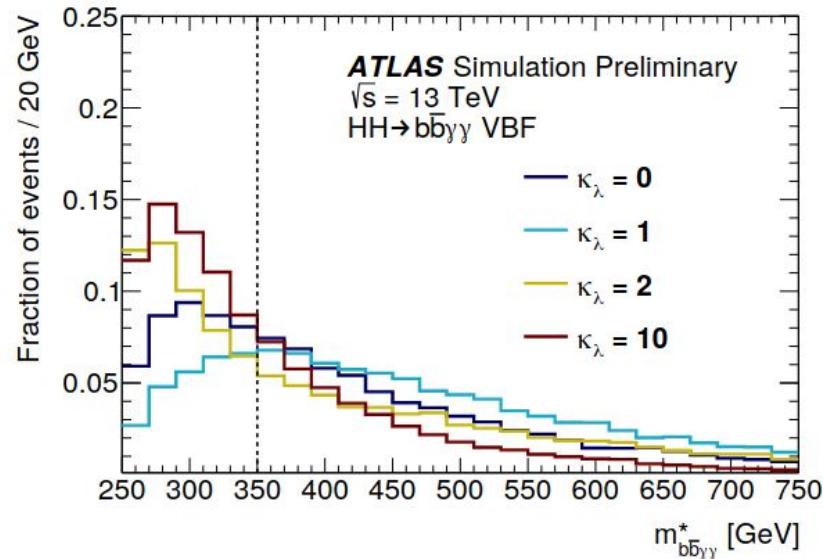


Figure 4: Reconstructed four-body mass for $m_X = 300 \text{ GeV}$ and $m_X = 500 \text{ GeV}$ resonant signal benchmarks and for the $\gamma\gamma$ +jets background. Dashed lines represent the distribution of $m_{b\bar{b}\gamma\gamma}$ while solid lines represent the distribution of $m_{b\bar{b}\gamma\gamma}^*$, defined in Section 4.2.1. Distributions are normalized to unit area.

$$m_{b\bar{b}\gamma\gamma}^* = m_{b\bar{b}\gamma\gamma} - m_{b\bar{b}} - m_{\gamma\gamma} + 250 \text{ GeV}$$



(a) ggF HH production mode



(b) VBF HH production mode

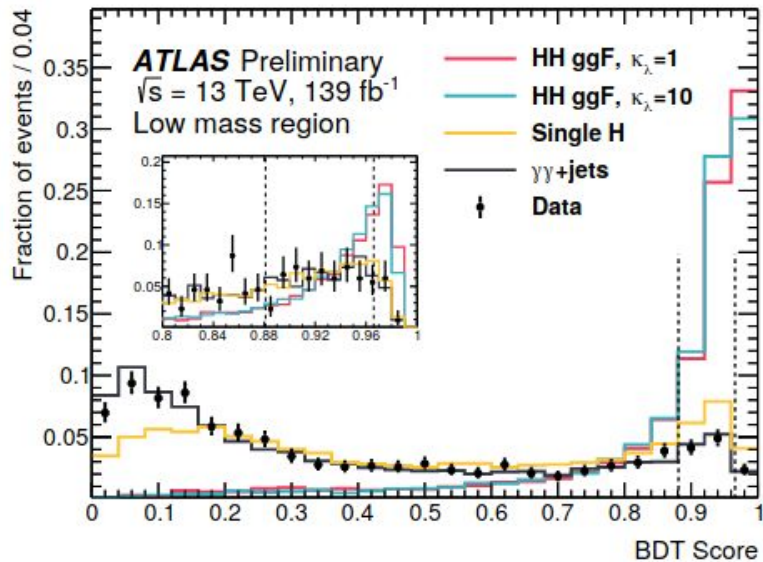
Figure 5: The $m_{b\bar{b}\gamma\gamma}^*$ distributions after the common preselection for (a) non-resonant ggF HH and (b) VBF HH signals with several κ_λ values. $m_{b\bar{b}\gamma\gamma}^* = 350 \text{ GeV}$ is chosen as the separating boundary between categories targeting the SM and BSM κ_λ signals.

Table 2: Variables used in the BDT for the non-resonant analysis. The b -tag status identifies the highest fixed b -tag working point (60%, 70%, 77%) that the jet passes. All vectors in the event are rotated so that the leading photon ϕ is equal to zero.

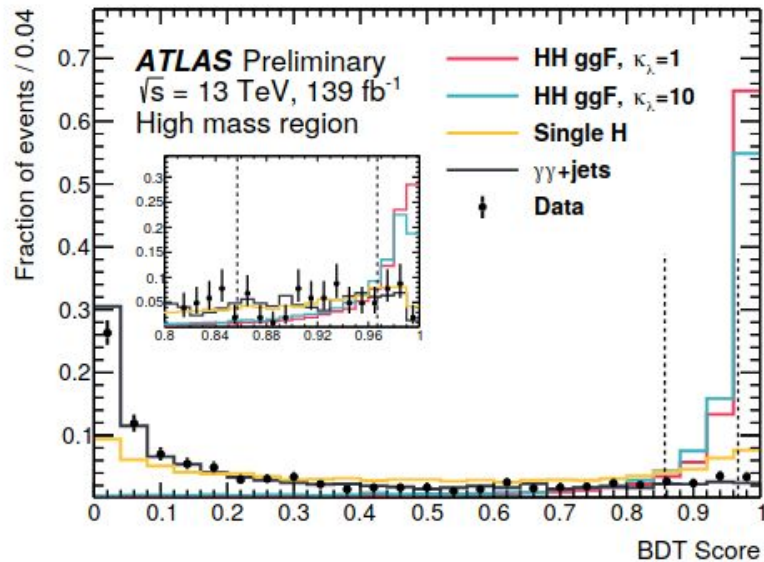
Variable	Definition
Photon-related kinematic variables	
$p_T/m_{\gamma\gamma}$	Transverse momentum of the two photons scaled by their invariant mass $m_{\gamma\gamma}$
η and ϕ	Pseudo-rapidity and azimuthal angle of the leading and sub-leading photon
Jet-related kinematic variables	
b -tag status	Highest fixed b -tag working point that the jet passes
p_T, η and ϕ	Transverse momentum, pseudo-rapidity and azimuthal angle of the two jets with the highest b -tagging score
$p_T^{b\bar{b}}, \eta_{b\bar{b}}$ and $\phi_{b\bar{b}}$	Transverse momentum, pseudo-rapidity and azimuthal angle of b -tagged jets system
$m_{b\bar{b}}$	Invariant mass built with the two jets with the highest b -tagging score
H_T	Scalar sum of the p_T of the jets in the event
Single topness	For the definition, see Eq. (1)
Missing transverse momentum-related variables	
E_T^{miss} and ϕ^{miss}	Missing transverse momentum and its azimuthal angle

Table 3: Definition of the categories used in the HH non-resonant search. Before entering the BDT-based categories, events are required to satisfy the common preselection.

Category	Selection criteria
High mass BDT tight	$m_{b\bar{b}\gamma\gamma}^* \geq 350 \text{ GeV}$, BDT score $\in [0.967, 1]$
High mass BDT loose	$m_{b\bar{b}\gamma\gamma}^* \geq 350 \text{ GeV}$, BDT score $\in [0.857, 0.967]$
Low mass BDT tight	$m_{b\bar{b}\gamma\gamma}^* < 350 \text{ GeV}$, BDT score $\in [0.966, 1]$
Low mass BDT loose	$m_{b\bar{b}\gamma\gamma}^* < 350 \text{ GeV}$, BDT score $\in [0.881, 0.966]$



(a) Low mass region

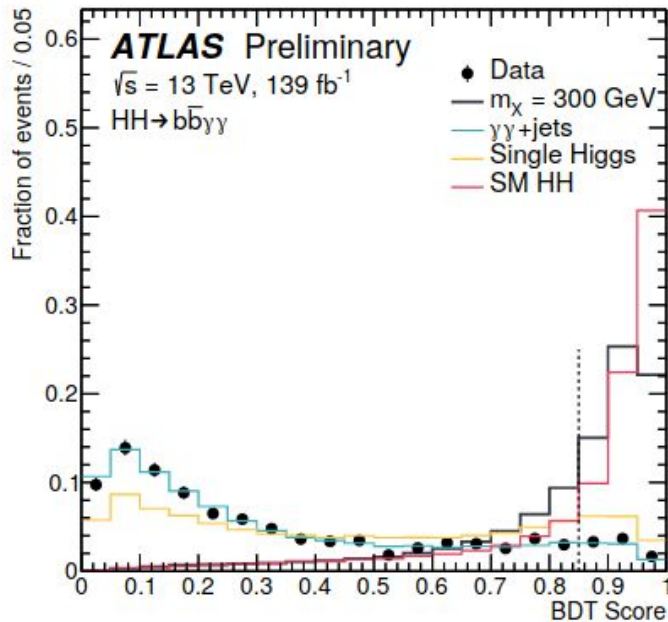


(b) High mass region

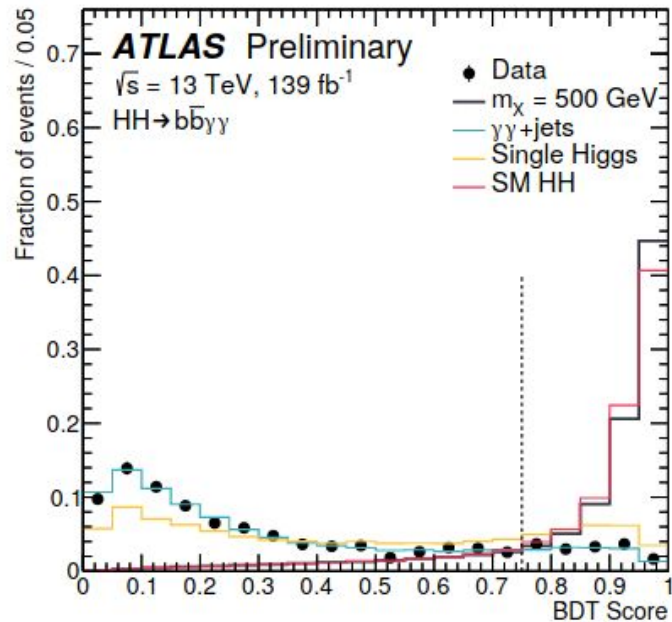
Figure 6: The BDT distribution of the di-Higgs ggF signal for two different values of k_λ and the main backgrounds in the (a) low and (b) high mass region. Distributions are normalized to unit area. The dotted lines denote the category boundaries. Events with a BDT score below 0.881 in the low mass region or below 0.857 in the high mass region are discarded.

Table 4: Variables used in the BDT for the resonant analysis. For variables depending on b -tagged jets, only jets b -tagged using the 77% working point are considered as described in Section 4.1.

Variable	Definition
Photon-related kinematic variables	
$p_T^{\gamma\gamma}, y^{\gamma\gamma}$	Transverse momentum and rapidity of the di-photon system
$\Delta\phi_{\gamma\gamma}$ and $\Delta R_{\gamma\gamma}$	Azimuthal angular distance and ΔR between the two photons
Jet-related kinematic variables	
$m_{b\bar{b}}, p_T^{b\bar{b}}$ and $y_{b\bar{b}}$	Invariant mass, transverse momentum and rapidity of the b -tagged jets system
$\Delta\phi_{b\bar{b}}$ and $\Delta R_{b\bar{b}}$	Azimuthal angular distance and ΔR between the two b -tagged jets
N_{jets} and $N_{b\text{-jets}}$	Number of jets and number of b -tagged jets
H_T	Scalar sum of the p_T of the jets in the event
Photons and jets-related kinematic variables	
$m_{b\bar{b}\gamma\gamma}$	Invariant mass built with the di-photon and b -tagged jets system
$\Delta y_{\gamma\gamma, b\bar{b}}, \Delta\phi_{\gamma\gamma, b\bar{b}}$ and $\Delta R_{\gamma\gamma, b\bar{b}}$	Distance in rapidity, azimuthal angle and ΔR between the di-photon and the b -tagged jets system

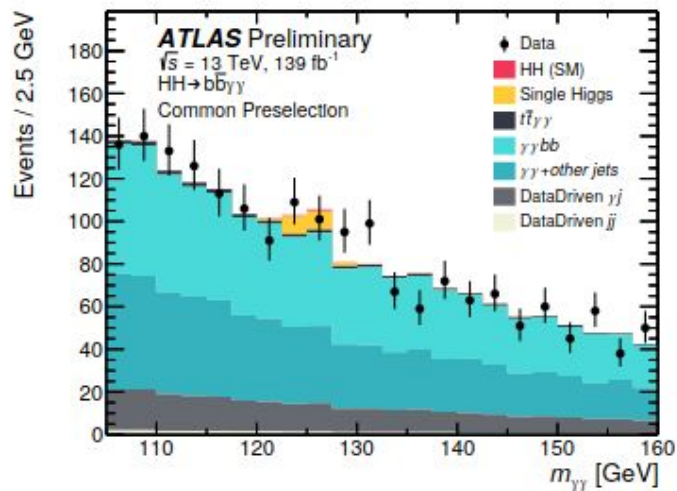


(a)

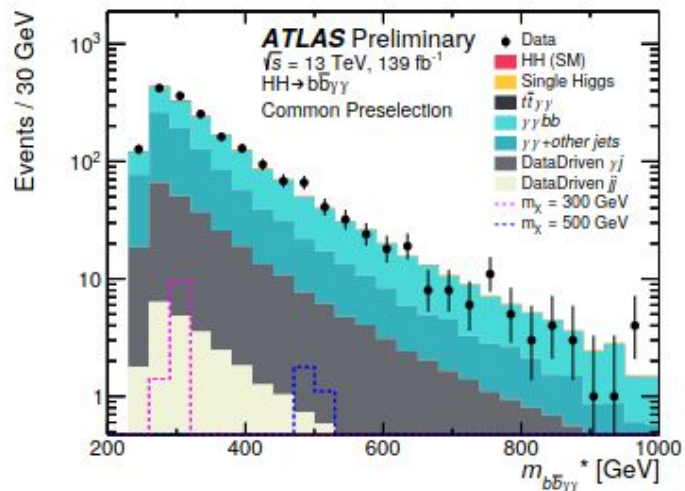


(b)

Figure 7: The BDT score for the benchmark signals ((a) $m_X = 300 \text{ GeV}$ and (b) $m_X = 500 \text{ GeV}$) and for the main backgrounds. Distributions are normalized to unit area. The dotted lines denote the event selection thresholds. Events with a BDT score below 0.85 for $m_X = 300 \text{ GeV}$ or below 0.75 for $m_X = 500 \text{ GeV}$ are discarded.

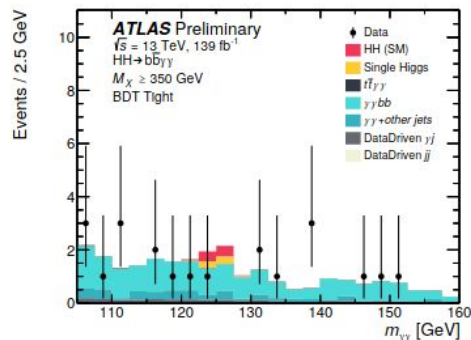


(a)

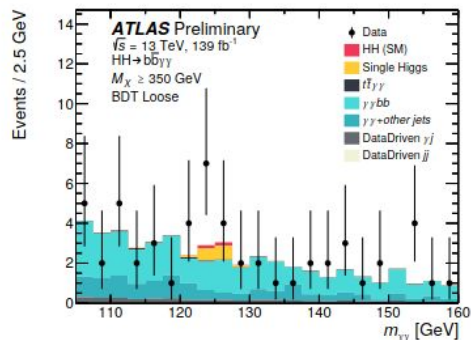


(b)

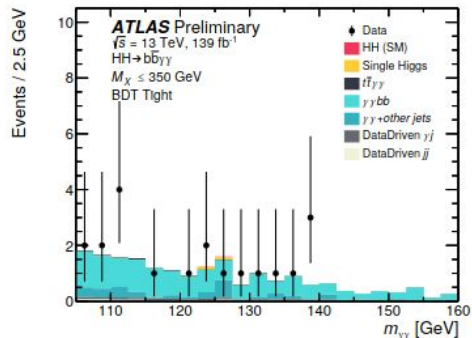
Figure 8: Distributions of (a) $m_{\gamma\gamma}$ and (b) $m_{b\bar{b}\gamma\gamma}^*$ for events passing the common preselection criteria. The continuum background is scaled by the $\gamma\gamma$, γ -jet or jet- γ , and di-jet fractions and normalized to the data sideband.



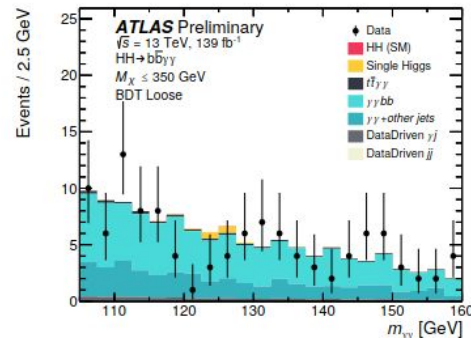
(a) High mass BDT tight selection



(b) High mass BDT loose selection

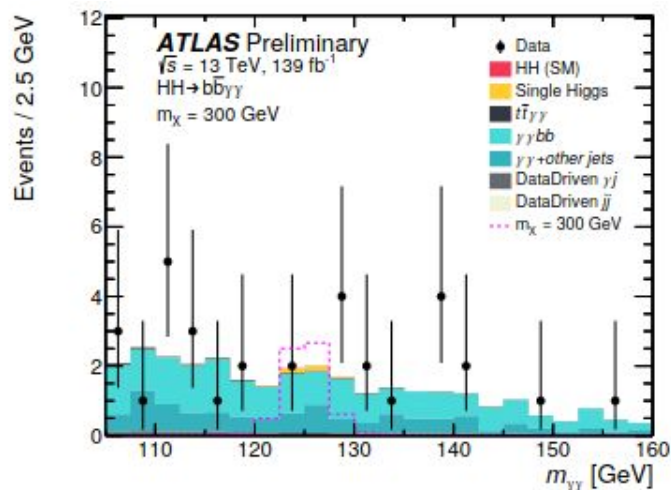


(c) Low mass BDT tight selection

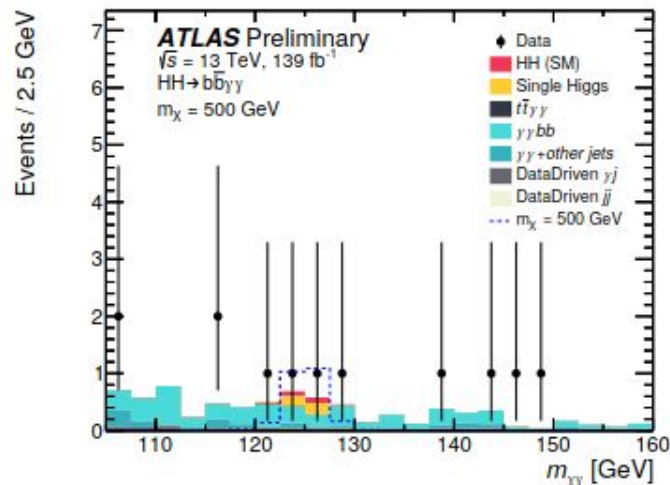


(d) Low mass BDT loose selection

Figure 9: Distributions of $m_{\gamma\gamma}$ in all signal categories for the non-resonant HH search: (a) high mass BDT tight, (b) high mass BDT loose, (c) low mass BDT tight, (d) low mass BDT loose. The continuum background is scaled by the $\gamma\gamma$, γ -jet, and di-jet fractions and normalized to the data sideband.



(a)



(b)

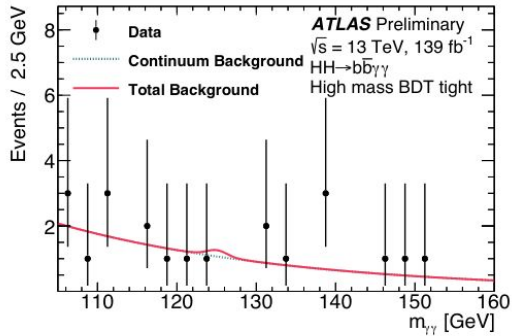
Figure 10: Distributions of $m_{\gamma\gamma}$ for the selections used for the resonance mass points (a) $m_X = 300$ GeV and (b) $m_X = 500$ GeV for the resonant search. The non-resonant background is scaled by the $\gamma\gamma$, γ -jet, and di-jet fractions and normalized to the data sideband. The scalar resonance signal is scaled to an arbitrary cross section value.

Likelihood function for bbyy:

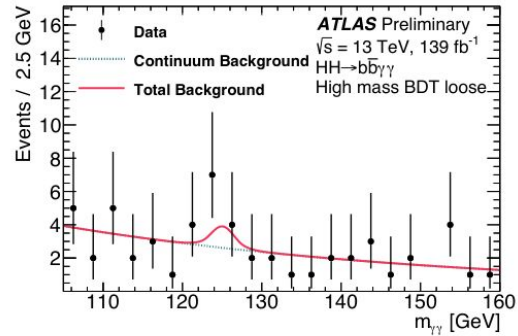
$$\mathcal{L} = \prod_c \left(\text{Pois}(n_c | N_c(\boldsymbol{\theta})) \cdot \prod_{i=1}^{n_c} f_c(m_{\gamma\gamma}^i, \boldsymbol{\theta}) \cdot G(\boldsymbol{\theta}) \right)$$

$$N_c(\boldsymbol{\theta}) = \mu \cdot N_{HH,c}(\boldsymbol{\theta}_{HH}^{\text{yield}}) + N_{\text{bkg},c}^{\text{res}}(\boldsymbol{\theta}_{\text{res}}^{\text{yield}}) + N_{\text{SS},c} \cdot \boldsymbol{\theta}^{\text{SS},c} + N_{\text{bkg},c}^{\text{non-res}}$$

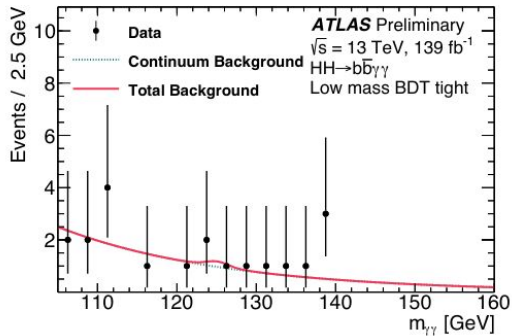
$$f_c(m_{\gamma\gamma}, \boldsymbol{\theta}) = [\mu \cdot N_{HH,c}(\boldsymbol{\theta}_{HH}^{\text{yield}}) \cdot f_{HH,c}(m_{\gamma\gamma}, \boldsymbol{\theta}_{HH}^{\text{shape}}) + N_{\text{bkg},c}^{\text{res}}(\boldsymbol{\theta}_{\text{res}}^{\text{yield}}) \cdot f_{\text{bkg},c}^{\text{res}}(m_{\gamma\gamma}, \boldsymbol{\theta}_{\text{res}}^{\text{shape}}) \\ + N_{\text{SS},c} \cdot \boldsymbol{\theta}_{HH}^{\text{SS},c} \cdot f_{HH,c}(m_{\gamma\gamma}, \boldsymbol{\theta}_{HH}^{\text{shape}}) + N_{\text{bkg},c}^{\text{non-res}} \cdot f_{\text{bkg},c}^{\text{non-res}}(m_{\gamma\gamma}, \boldsymbol{\theta}_{\text{non-res}}^{\text{shape}})] / N_c(\boldsymbol{\theta}_{\text{non-res}}^{\text{yield}})$$



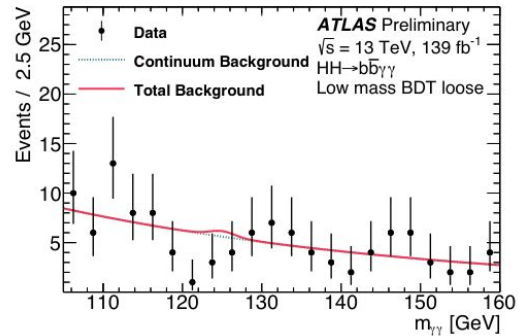
(a) High mass BDT tight



(b) High mass BDT loose



(c) Low mass BDT tight



(d) Low mass BDT loose

Figure 11: Data are compared to the background-only fit for the four categories of the non-resonant search. Both the continuum background and the background from single Higgs boson production are considered.

Table 6: Expected and observed numbers of events in the categories of the non-resonant search. An additional requirement of $120 \text{ GeV} < m_{\gamma\gamma} < 130 \text{ GeV}$ is applied. The uncertainties on the continuum background are those arising from the fitting procedure. The uncertainties on the single Higgs boson and Higgs boson pair productions are from MC statistical error.

	High mass BDT tight	High mass BDT loose	Low mass BDT tight	Low mass BDT loose
Continuum background	4.9 ± 1.1	9.5 ± 1.5	3.7 ± 1.0	24.9 ± 2.5
Single Higgs boson background	0.670 ± 0.032	1.57 ± 0.04	0.220 ± 0.016	1.39 ± 0.04
ggF	0.261 ± 0.028	0.44 ± 0.04	0.063 ± 0.014	0.274 ± 0.030
$i\bar{i}H$	0.1929 ± 0.0045	0.491 ± 0.007	0.1074 ± 0.0033	0.742 ± 0.009
ZH	0.142 ± 0.005	0.486 ± 0.010	0.04019 ± 0.0027	0.269 ± 0.007
Rest	0.074 ± 0.012	0.155 ± 0.020	0.008 ± 0.006	0.109 ± 0.016
SM HH signal	0.8753 ± 0.0032	0.3680 ± 0.0020	$(49.4 \pm 0.7) \cdot 10^{-3}$	$(78.7 \pm 0.9) \cdot 10^{-3}$
ggF	0.8626 ± 0.0032	0.3518 ± 0.0020	$(46.1 \pm 0.7) \cdot 10^{-3}$	$(71.8 \pm 0.9) \cdot 10^{-3}$
VBF	0.01266 ± 0.00016	0.01618 ± 0.00018	$(3.22 \pm 0.08) \cdot 10^{-3}$	$(6.923 \pm 0.011) \cdot 10^{-3}$
Alternative $HH(\kappa_\lambda = 10)$ signal	6.36 ± 0.05	3.691 ± 0.038	4.65 ± 0.04	8.64 ± 0.06
Data	2	17	5	14

Table 8: Breakdown of the dominant systematic uncertainties. The impact of the uncertainties is defined according to the statistical analysis described in Section 7. It corresponds to the variation on the upper limit on the signal strength when re-evaluating the profile likelihood ratio after fixing the nuisance parameter in question to its best-fit value increased or decreased by one standard deviation, while all remaining nuisance parameters remain free to float. The impact is shown in %. Only systematic uncertainties with an impact of at least 0.5% are shown. Uncertainties of Norm. + Shape type have effects on both the normalization and the parameters of the functional form, the rest of uncertainties affects only the yields.

		Relative impact of the systematic uncertainties in %	
Source	Type	Non-resonant analysis HH	Resonant analysis $m_X = 300$ GeV
Experimental			
Photon energy scale	Norm. + Shape	5.2	2.7
Photon energy resolution	Norm. + Shape	1.8	1.6
Flavor tagging	Normalization	0.5	< 0.5
Theoretical			
Heavy flavor content	Normalization	1.5	< 0.5
Higgs boson mass	Norm. + Shape	1.8	< 0.5
PDF+ α_s	Normalization	0.7	< 0.5
Spurious signal	Normalization	5.5	5.4

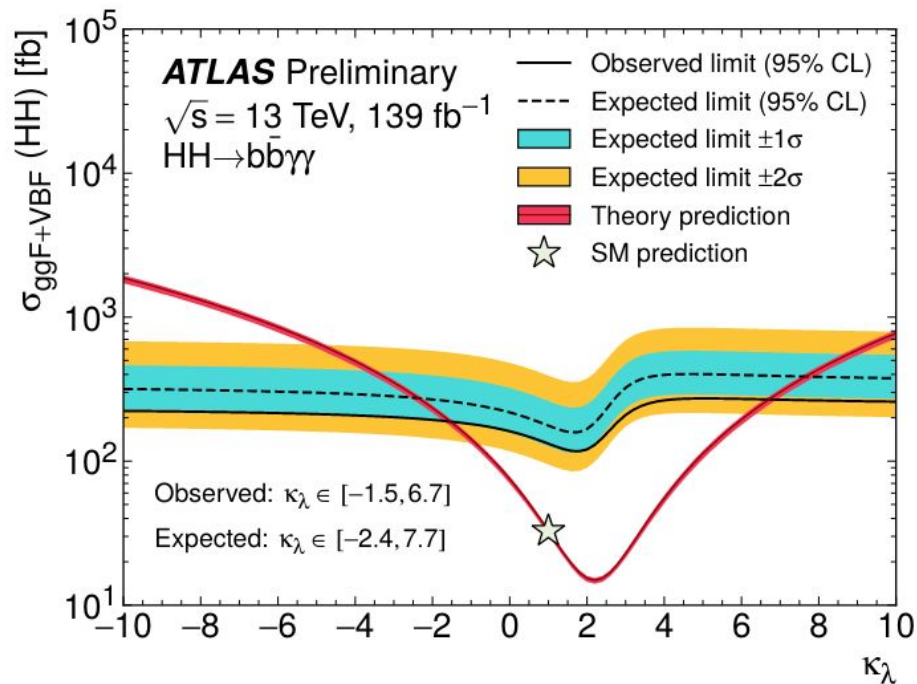
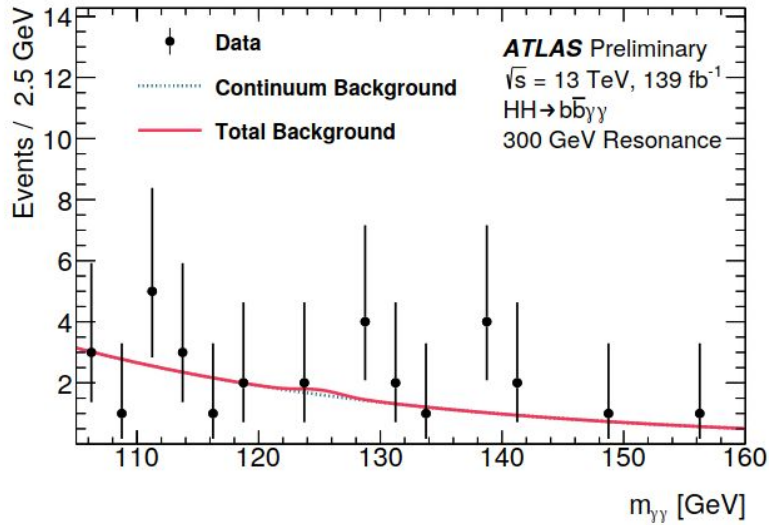


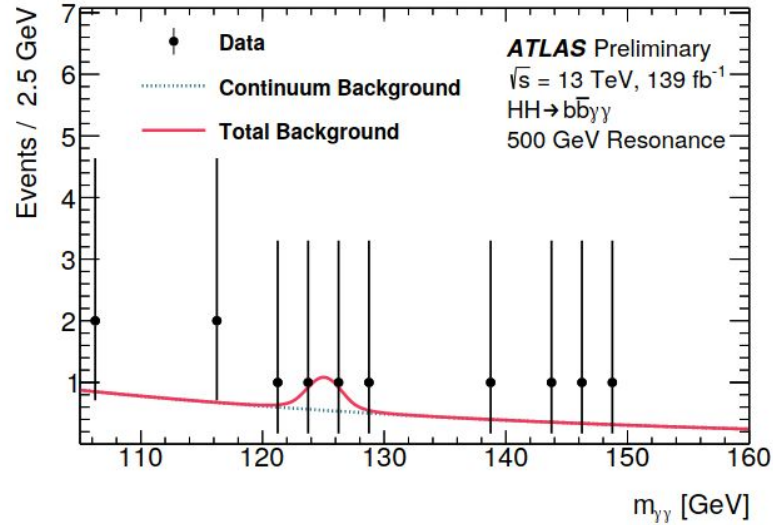
Figure 12: Observed and expected limits at 95% CL on the cross section of non-resonant Higgs boson pair production as a function of the Higgs boson self-coupling modifier $\kappa_\lambda = \lambda_{HHH} / \lambda_{HHH}^{\text{SM}}$. The constraints on κ_λ are obtained over an expected hypothesis excluding $pp \rightarrow HH$ production. The $\pm 1\sigma$ and $\pm 2\sigma$ variations about the expected limit due to statistical and systematic uncertainties are also shown. The theory prediction curve represents the scenario where all parameters and couplings are set to their SM values except for κ_λ . The uncertainty band of the theory prediction curve shows the cross section uncertainty.

Table 7: Expected and observed numbers of events of the resonant HH search. An additional requirement of $120 \text{ GeV} < m_{\gamma\gamma} < 130 \text{ GeV}$ is applied. The event numbers quoted for the scalar resonance signal assume an arbitrary total production cross section $\sigma(pp \rightarrow X \rightarrow HH)$ equal to the observed exclusion limits of Figure 14. The uncertainties on the continuum background are those arising from the fitting procedure. The uncertainties on the single Higgs boson, Higgs boson pair and scalar resonance production are from the MC statistical error.

	$m_X = 300 \text{ GeV}$	$m_X = 500 \text{ GeV}$
Continuum background	5.6 ± 2.4	3.5 ± 2.0
Single Higgs boson background	0.339 ± 0.009	0.398 ± 0.010
SM HH background	$(20.6 \pm 0.5) \cdot 10^{-3}$	0.1932 ± 0.0015
$X \rightarrow HH$ signal	5.771 ± 0.031	5.950 ± 0.026
Data	6	4



(a)



(b)

Figure 13: Data are compared to the background-only fit for the resonant search for the (a) $m_X = 300$ GeV and (b) $m_X = 500$ GeV mass hypotheses. The continuum background, as well as the background from single Higgs boson production and from the SM HH production are considered.

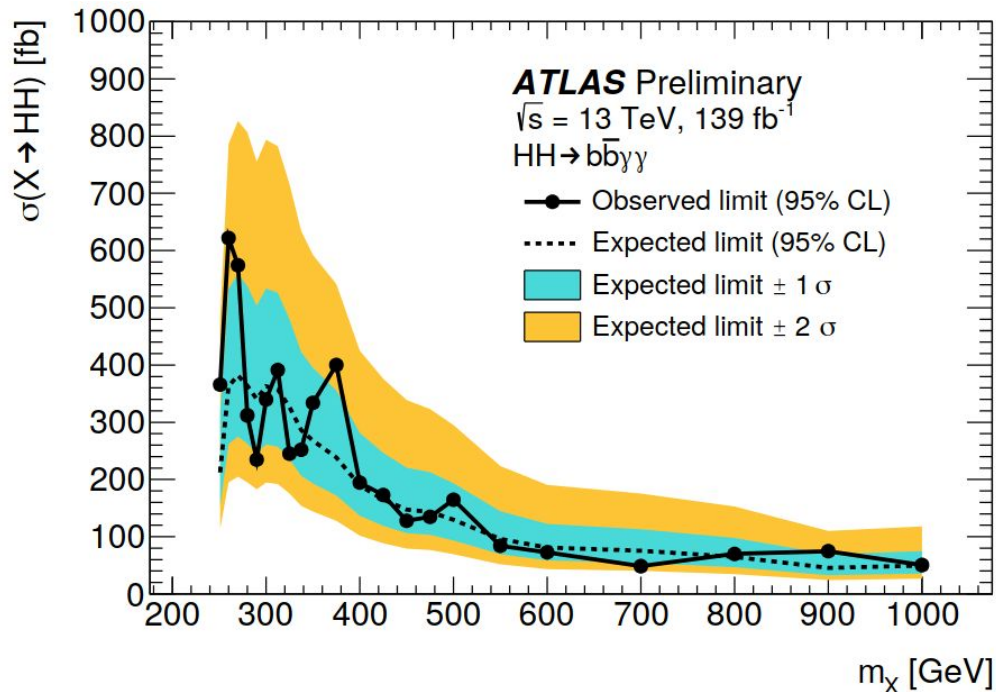


Figure 14: Observed and expected limits at 95% CL on the production cross section of a narrow width scalar resonance X as a function of the mass m_X of the hypothetical scalar particle. The black solid line represents the observed upper limits. The dashed line represents the expected upper limits. The $\pm 1\sigma$ and $\pm 2\sigma$ variations about the expected limit due to statistical and systematic uncertainties are also shown.

HH \rightarrow bb $\tau\tau$

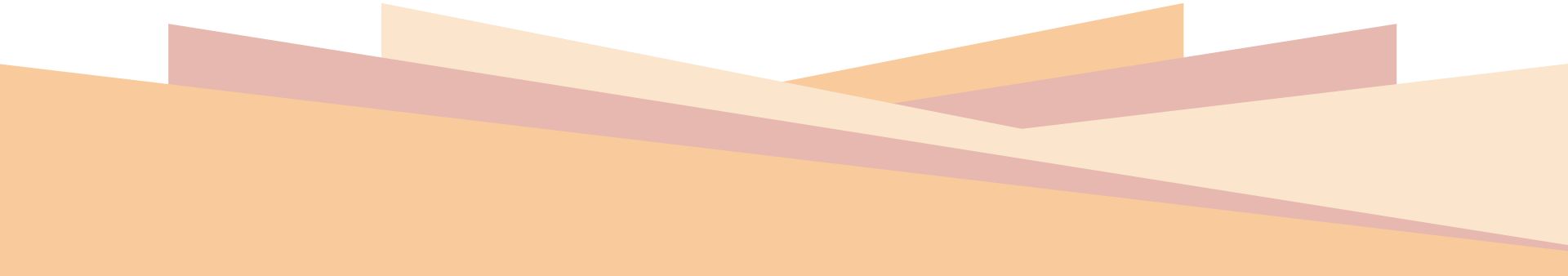


Table 2: Summary of the event selections, shown separately in the different trigger categories. In cases where pairs of reconstructed objects of the same type are required, thresholds on the (sub-)leading p_T object are given outside (within) parentheses. When the selection depends on the year of data-taking, the possible values of the requirements are separated by commas, except for the jet selection in the lepton-plus- $\tau_{\text{had-vis}}$ trigger and di- $\tau_{\text{had-vis}}$ triggers, which use multiple selection criteria as described in Section 5.1. The trigger p_T thresholds shown correspond to the offline requirements.

$\tau_{\text{had}} \tau_{\text{had}}$ category		$\tau_{\text{lep}} \tau_{\text{had}}$ categories		
STT	DTT	SLT	LTT	
e/μ selection				
No loose e/μ with $p_T > 7$ GeV		Exactly one tight e or medium μ		
		$p_T^e > 25, 27$ GeV	$18 \text{ GeV} < p_T^e < \text{SLT cut}$	
		$p_T^\mu > 21, 27$ GeV	$15 \text{ GeV} < p_T^\mu < \text{SLT cut}$	
		$ \eta^e < 2.47$, not $1.37 < \eta^e < 1.52$		
		$ \eta^\mu < 2.7$		
$\tau_{\text{had-vis}}$ selection				
Two loose $\tau_{\text{had-vis}}$		One loose $\tau_{\text{had-vis}}$		
$ \eta < 2.5$		$ \eta < 2.3$		
$p_T > 100, 140, 180$ (25) GeV	$p_T > 40$ (30) GeV	$p_T > 20$ GeV	$p_T > 30$ GeV	
Jet selection				
≥ 2 jets with $ \eta < 2.5$				
$p_T > 45$ (20) GeV	Trigger dependent	$p_T > 45$ (20) GeV	Trigger dependent	
Event-level selection				
Trigger requirements passed				
Collision vertex reconstructed				
$m_{\tau\tau}^{\text{MMC}} > 60$ GeV				
Opposite-sign electric charges of $e/\mu/\tau_{\text{had-vis}}$ and $\tau_{\text{had-vis}}$				
Exactly two b -tagged jets				
$m_{bb} < 150$ GeV				

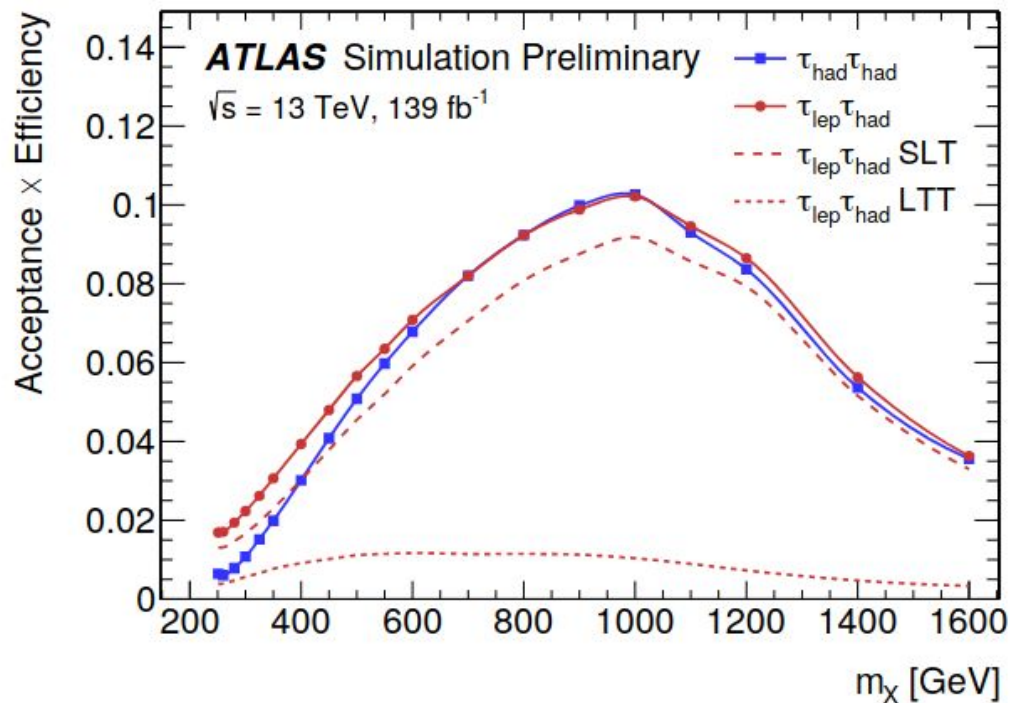
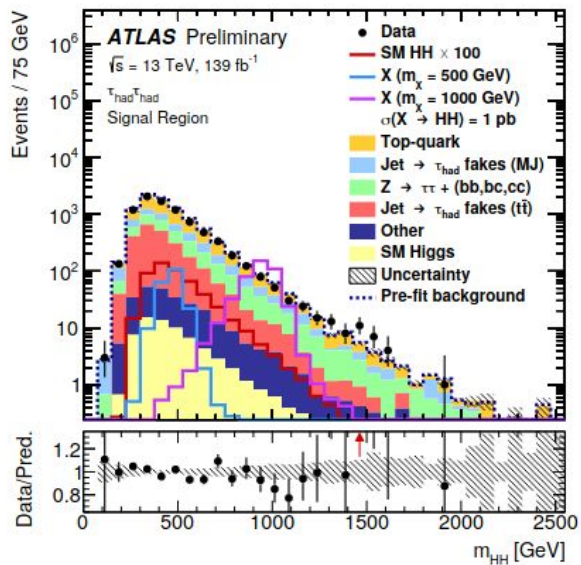


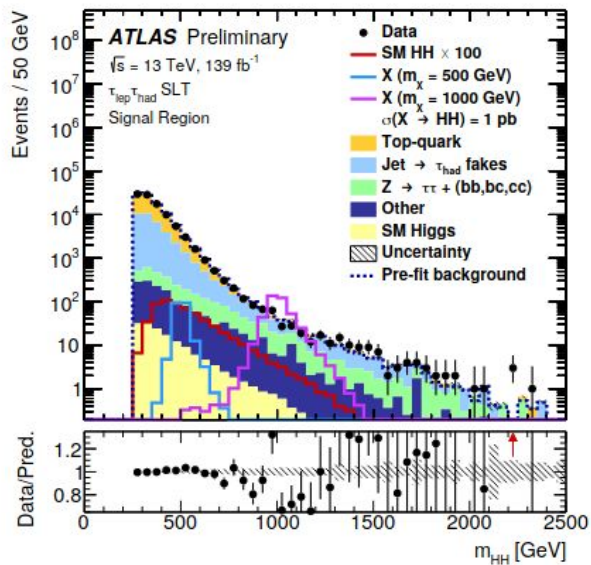
Figure 2: Acceptance times efficiency for the full analysis selection as a function of the resonance mass m_X in the $\tau_{\text{had}}\tau_{\text{had}}$, $\tau_{\text{lep}}\tau_{\text{had}}$ single-lepton trigger and $\tau_{\text{lep}}\tau_{\text{had}}$ lepton-plus- $\tau_{\text{had-vis}}$ trigger categories, shown in solid line with square markers, dashed and dotted lines, respectively. The solid line with circle markers is the acceptance times efficiency curve for the combined $\tau_{\text{lep}}\tau_{\text{had}}$ category. The acceptance times efficiency is evaluated for $X \rightarrow HH \rightarrow b\bar{b}\tau^+\tau^-$ decays, with respect to the targeted τ -lepton decay modes ($\tau_{\text{lep}}\tau_{\text{had}}$ or $\tau_{\text{had}}\tau_{\text{had}}$).

Table 3: Variables used as inputs to the MVAs in the three analysis categories. The same choice of input variables is used for the resonant and non-resonant production modes. The variables are defined in the main text.

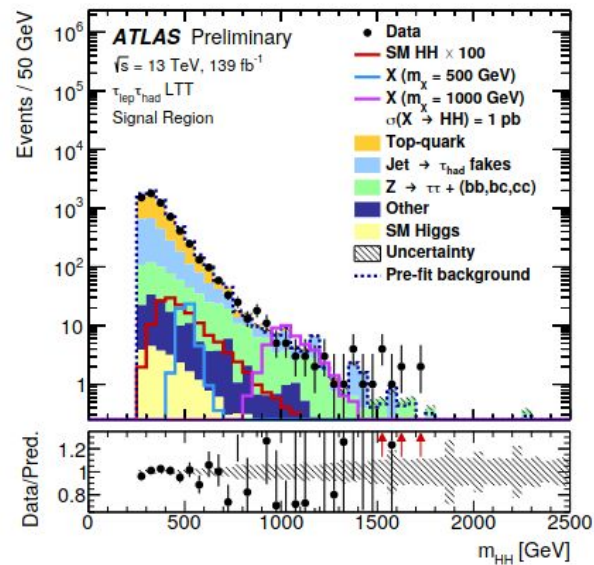
Variable	$\tau_{\text{had}} \tau_{\text{had}}$	$\tau_{\text{lep}} \tau_{\text{had}}$ SLT	$\tau_{\text{lep}} \tau_{\text{had}}$ LTT
m_{HH}	✓	✓	✓
$m_{\tau\tau}^{\text{MMC}}$	✓	✓	✓
m_{bb}	✓	✓	✓
$\Delta R(\tau, \tau)$	✓	✓	✓
$\Delta R(b, b)$	✓	✓	
$\Delta p_{\text{T}}(\ell, \tau)$		✓	✓
Sub-leading b -tagged jet p_{T}		✓	
m_{T}^{W}		✓	
$E_{\text{T}}^{\text{miss}}$		✓	
$\mathbf{p}_{\text{T}}^{\text{miss}}$ ϕ centrality		✓	
$\Delta\phi(\ell\tau, bb)$		✓	
$\Delta\phi(\ell, \mathbf{p}_{\text{T}}^{\text{miss}})$			✓
$\Delta\phi(\ell\tau, \mathbf{p}_{\text{T}}^{\text{miss}})$			✓
S_{T}			✓



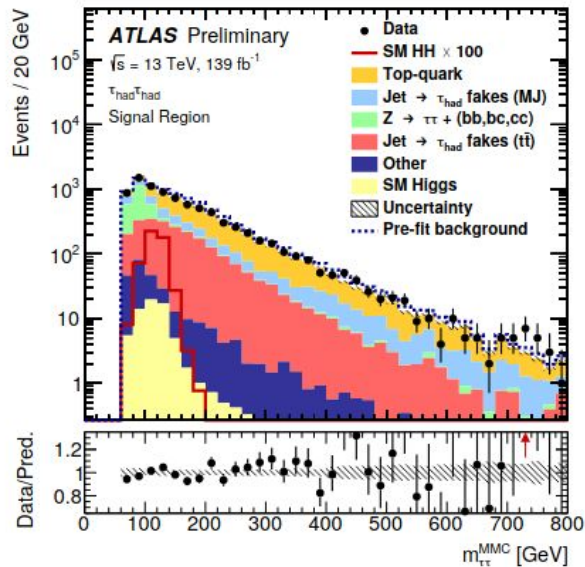
(a)



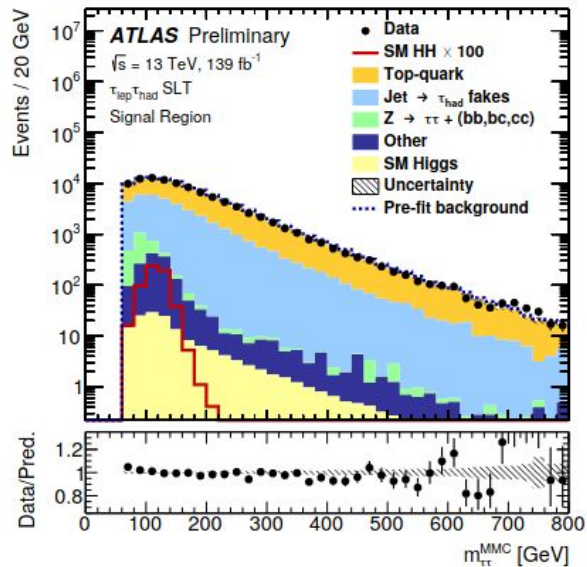
(b)



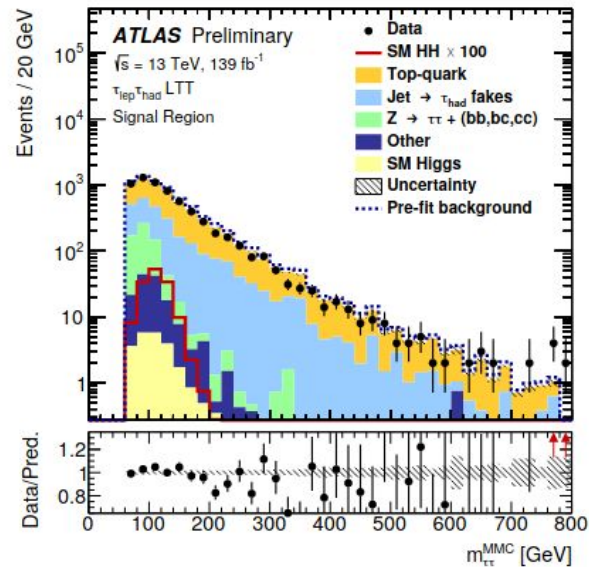
(c)



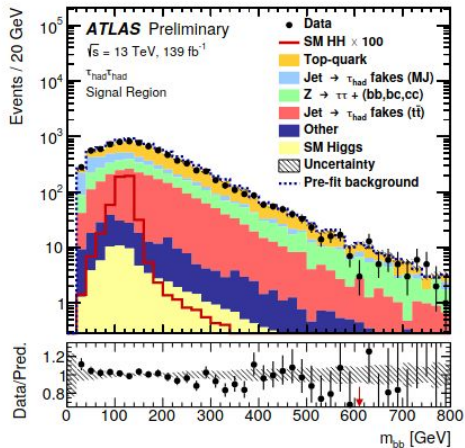
(d)



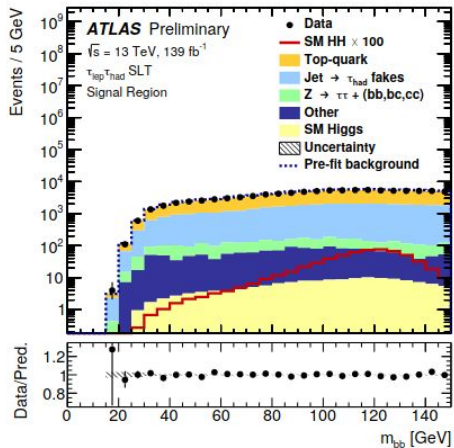
(e)



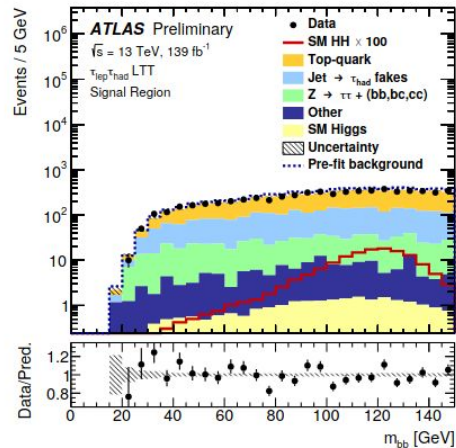
(f)



(g)



(h)



(i)

Figure 3: Signal (solid lines), post-fit background (filled histograms) and data (dots with error bars) distributions of m_{HH} (top), $m_{\tau\tau}^{\text{MMC}}$ (middle row) and m_{bb} (bottom) for events in the $\tau_{\text{had}}\tau_{\text{had}}$ (left), $\tau_{\text{lep}}\tau_{\text{had}}$ single-lepton trigger (middle column) and $\tau_{\text{lep}}\tau_{\text{had}}$ lepton-plus- $\tau_{\text{had-vis}}$ trigger (right) categories. The normalisation and shape of the backgrounds and the uncertainty on the total background shown are determined from the likelihood fit to data in the non-resonant HH search. The expected non-resonant signal is overlaid with its normalisation scaled by a factor of 100, and the $m_X = 500$ GeV and $m_X = 1000$ GeV resonant signals are overlaid in the m_{HH} distributions with their cross-section set to 1 pb. The dashed histogram shows the total pre-fit background. The size of the combined statistical and systematic uncertainty of the background is indicated by the hatched band. The ratio of the data to the sum of the backgrounds is shown in the lower panels.

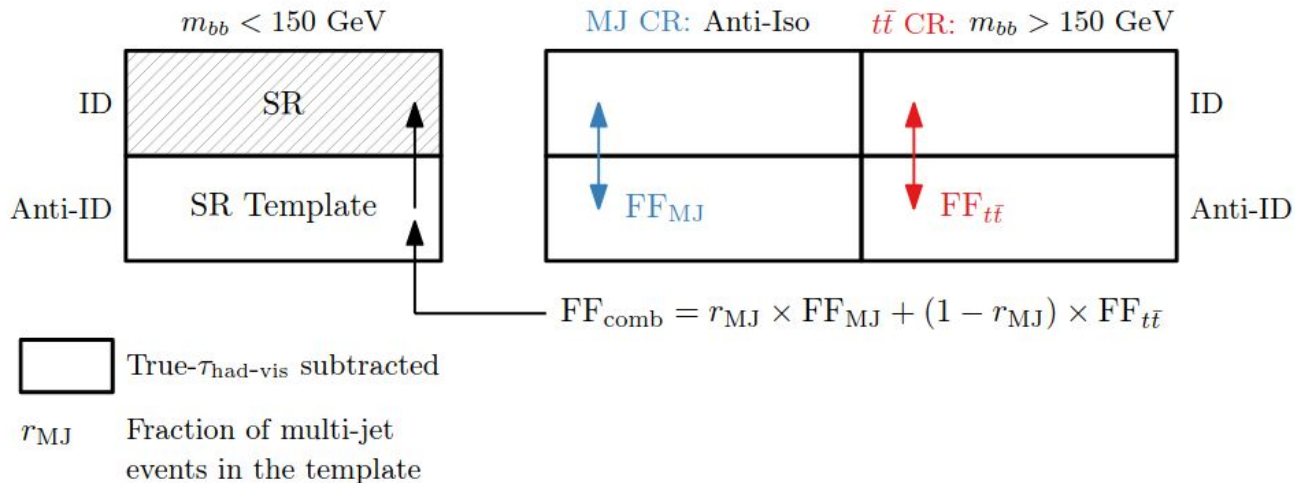


Figure 4: Schematic depiction of the combined fake-factor method used to estimate multi-jet and $t\bar{t}$ backgrounds with fake- $\tau_{\text{had-vis}}$ in the $\tau_{\text{lep}}\tau_{\text{had}}$ channel. Backgrounds which are not from events with fake- $\tau_{\text{had-vis}}$ originating from jets are estimated from simulation and are subtracted from data in all control regions. Events in which an electron or a muon is misidentified as a $\tau_{\text{had-vis}}$ are also subtracted, but their contribution is very small. Both sources are indicated by "True- $\tau_{\text{had-vis}}$ subtracted" in the legend.

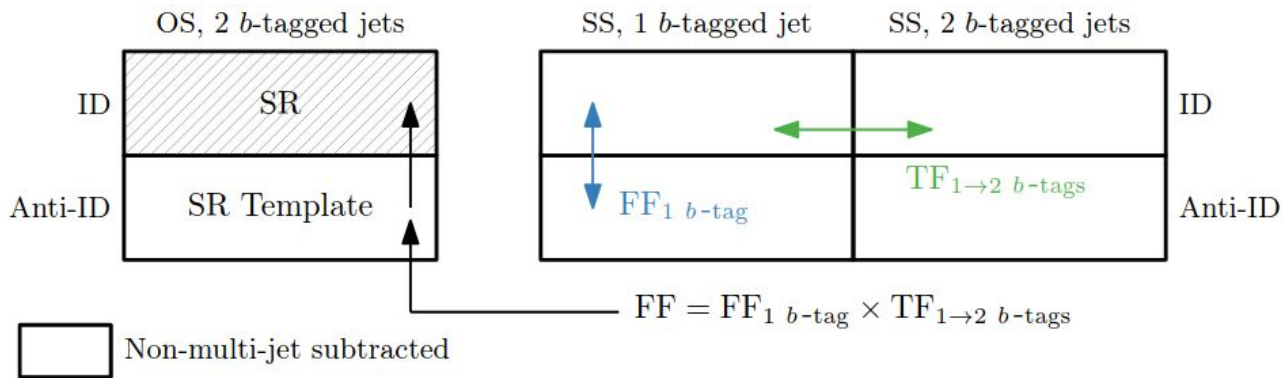
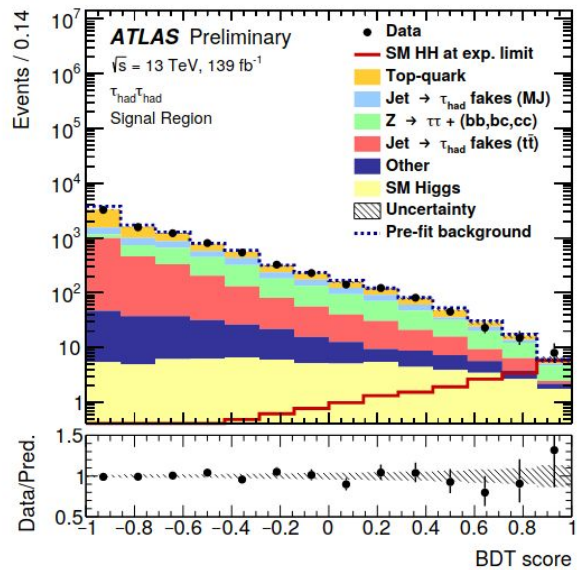


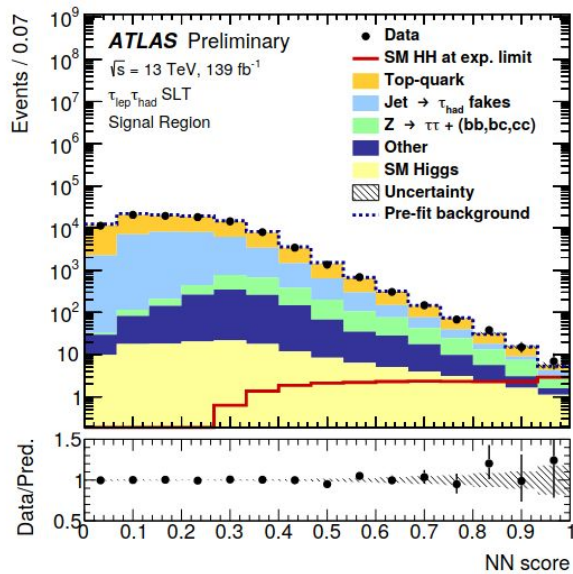
Figure 5: Schematic depiction of the combined fake-factor method to estimate the multi-jet background with fake- $\tau_{\text{had-vis}}$ in the $\tau_{\text{had}}\tau_{\text{had}}$ channel. Backgrounds with true- $\tau_{\text{had-vis}}$ that are not from multi-jet events are simulated and subtracted from data in all the control regions. This is indicated by "Non-multi-jet subtracted" in the legend.

Table 4: Breakdown of the relative contributions to the uncertainty in the extracted signal cross-sections, as determined in the likelihood fit to data. These are obtained by fixing the relevant nuisance parameters in the likelihood fit, and subtracting the obtained uncertainty on the fitted signal cross-sections in quadrature from the total uncertainty, and then dividing the result by the total uncertainty. The sum in quadrature of the individual components differs from the total uncertainty due to correlations between the groups of uncertainties.

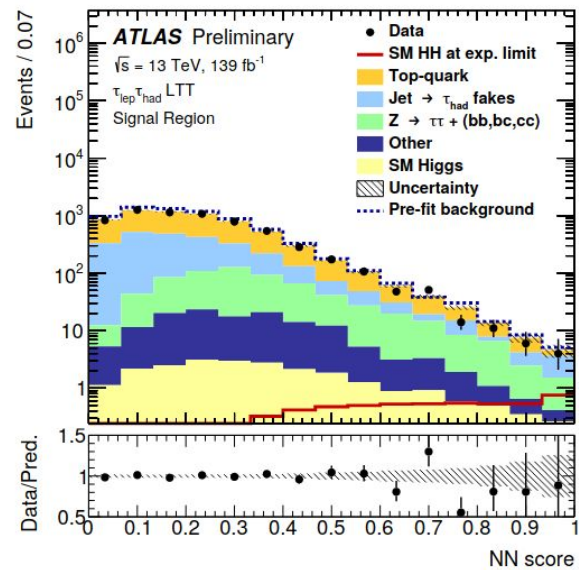
Uncertainty source	Non-resonant HH	Resonant $X \rightarrow HH$		
		300 GeV	500 GeV	1000 GeV
Data statistical	81%	75%	89%	88%
Systematic	59%	66%	46%	48%
$t\bar{t}$ and Z + HF normalisations	4%	15%	3%	3%
MC statistical	28%	44%	33%	18%
Experimental				
Jet and E_T^{miss}	7%	28%	5%	3%
b -jet tagging	3%	6%	3%	3%
$\tau_{\text{had-vis}}$	5%	13%	3%	7%
Electrons and muons	2%	3%	2%	1%
Luminosity and pileup	3%	2%	2%	5%
Theoretical and modelling				
Fake- $\tau_{\text{had-vis}}$	9%	22%	8%	7%
Top-quark	24%	17%	15%	8%
$Z(\rightarrow \tau\tau)$ + HF	9%	17%	9%	15%
Single Higgs boson	29%	2%	15%	14%
Other backgrounds	3%	2%	5%	3%
Signal	5%	15%	13%	34%



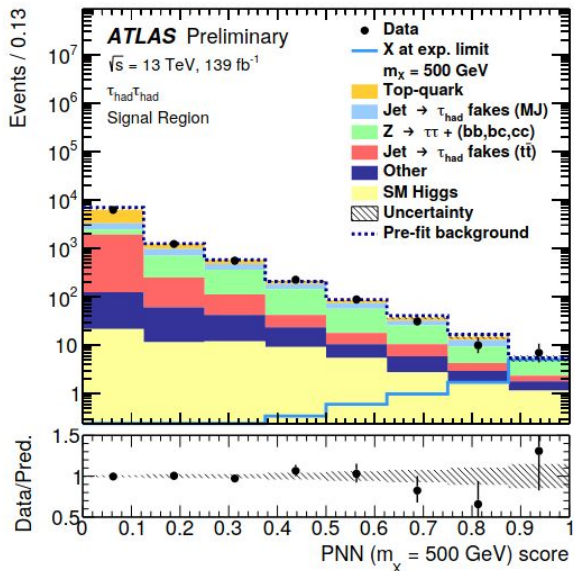
(a)



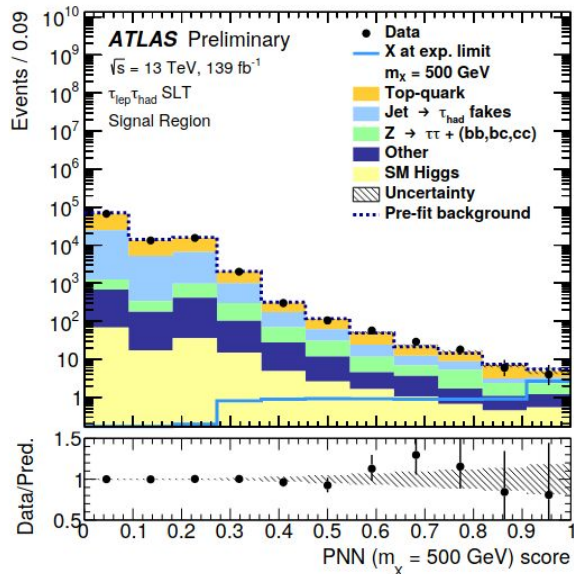
(b)



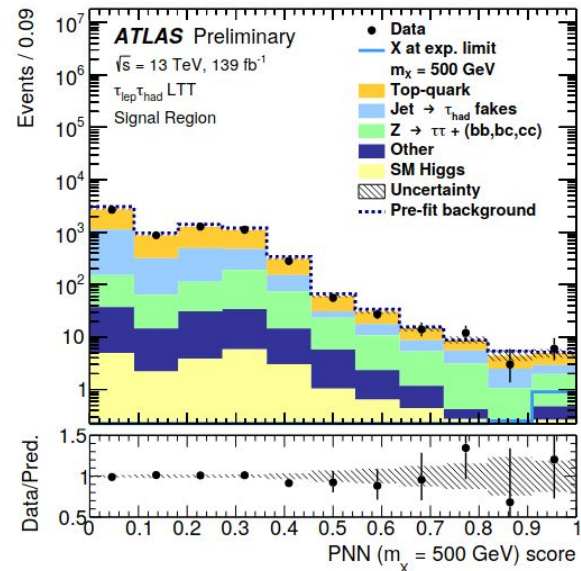
(c)



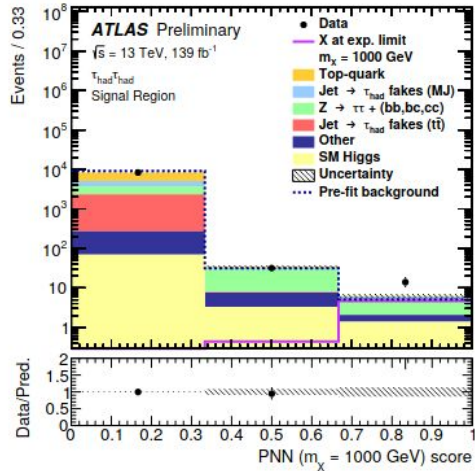
(d)



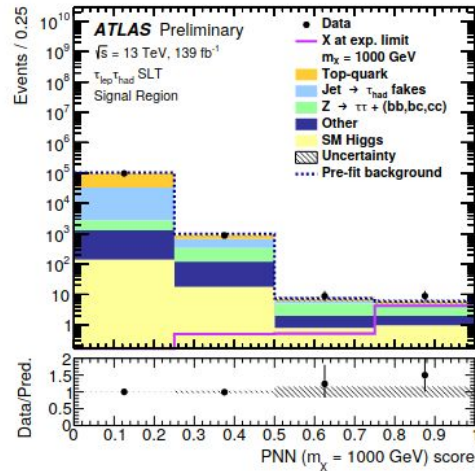
(e)



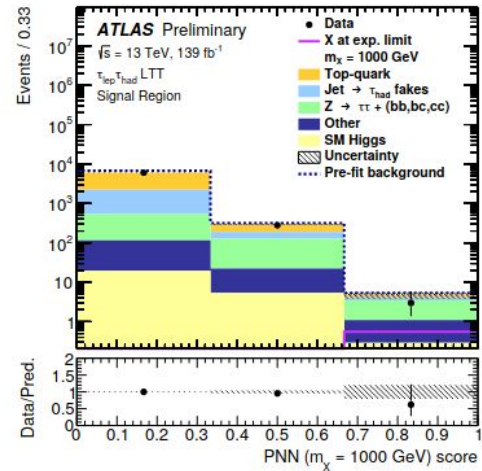
(f)



(g)



(h)



(i)

Figure 7: The MVA output distributions in the search for non-resonant HH signal (top) and in the search for resonant HH signal with $m_X = 500$ GeV (middle row) and $m_X = 1000$ GeV (bottom), in the $\tau_{\text{had}}\tau_{\text{had}}$ (left), $\tau_{\text{lep}}\tau_{\text{had}}$ single-lepton trigger (middle column) and $\tau_{\text{lep}}\tau_{\text{had}}$ lepton-plus- $\tau_{\text{had-vis}}$ trigger (right) categories. The distributions are shown after the fit to the background-only hypothesis. The signal is overlaid and scaled to the combined expected limit. The dashed histogram shows the total pre-fit background. The lower panels show the ratio between data and the total post-fit background, where the hatched band shows the statistical and systematic uncertainties on that background. For visualisation purposes, these histograms are displayed using uniform bin widths instead of the bin edges used in the fit, though the bin contents correspond to those used in the fit.

Table 5: Observed and expected upper limits at 95% CL on the cross-section of non-resonant HH production according to SM-like kinematics, and on the cross-section of non-resonant HH production divided by the SM prediction. The $\pm 1 \sigma$ and $\pm 2 \sigma$ variations around the expected limit are also shown.

		Observed	-2σ	-1σ	Expected	$+1 \sigma$	$+2 \sigma$
$\tau_{\text{had}} \tau_{\text{had}}$	$\sigma_{\text{ggF+VBF}}$ [fb]	145	70.5	94.6	131	183	245
	$\sigma_{\text{ggF+VBF}}/\sigma_{\text{ggF+VBF}}^{\text{SM}}$	4.95	2.38	3.19	4.43	6.17	8.27
$\tau_{\text{lep}} \tau_{\text{had}}$	$\sigma_{\text{ggF+VBF}}$ [fb]	265	124	167	231	322	432
	$\sigma_{\text{ggF+VBF}}/\sigma_{\text{ggF+VBF}}^{\text{SM}}$	9.16	4.22	5.66	7.86	10.9	14.7
Combined	$\sigma_{\text{ggF+VBF}}$ [fb]	135	61.3	82.3	114	159	213
	$\sigma_{\text{ggF+VBF}}/\sigma_{\text{ggF+VBF}}^{\text{SM}}$	4.65	2.08	2.79	3.87	5.39	7.22

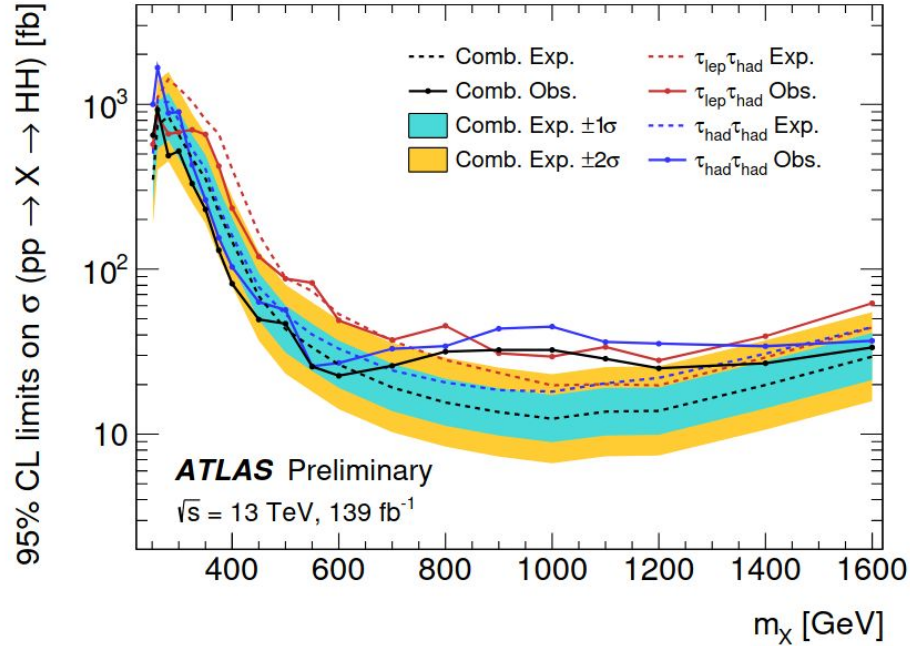
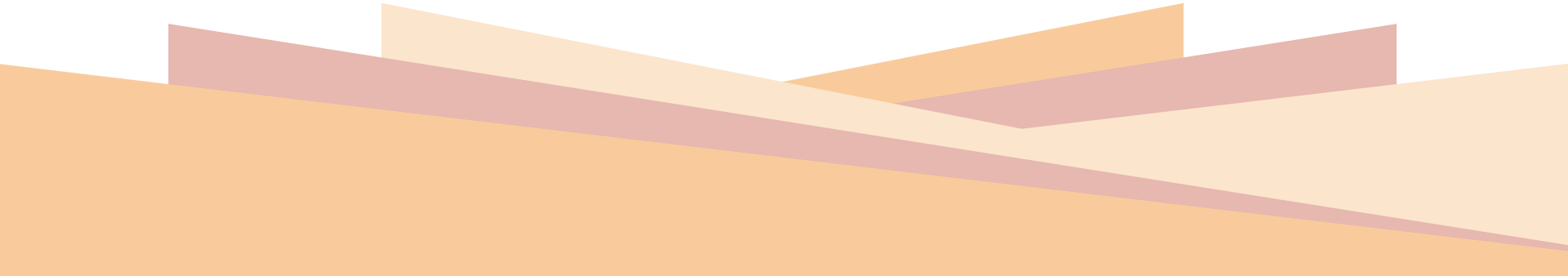


Figure 8: Observed and expected limits at 95% CL on the cross-section of the resonant HH production as a function of the scalar resonance mass m_X . The dashed lines show the expected limits while the solid lines show the observed limits. The blue and red lines are the limits for the $\tau_{\text{had}}\tau_{\text{had}}$ channel and $\tau_{\text{lep}}\tau_{\text{had}}$ channel, respectively. The black lines are the combined limits of the two channels. The $\pm 1\sigma$ and $\pm 2\sigma$ variations around the expected combined limit are indicated by the turquoise and yellow bands, respectively. The limits are obtained using the profile-likelihood test statistic and the modified frequentist CL_s technique.

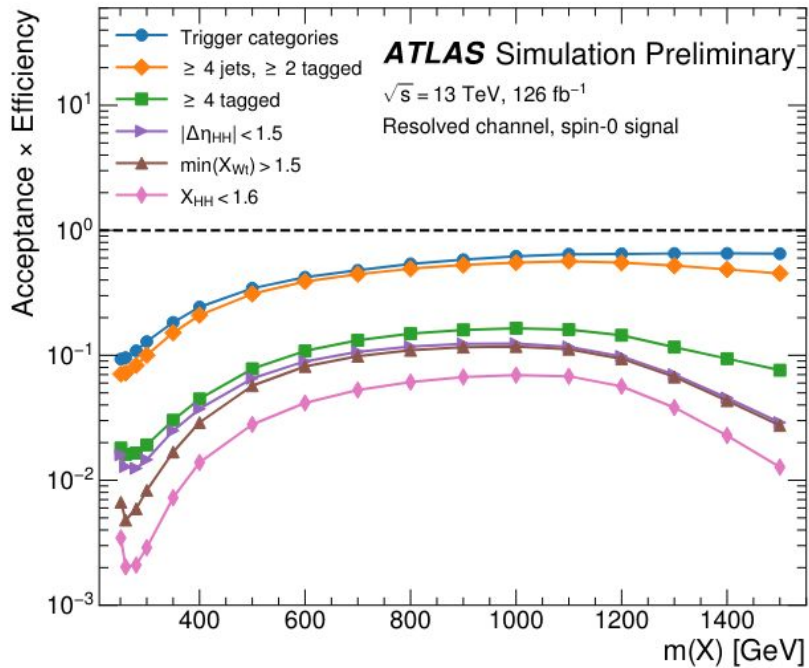
HH → bbbb



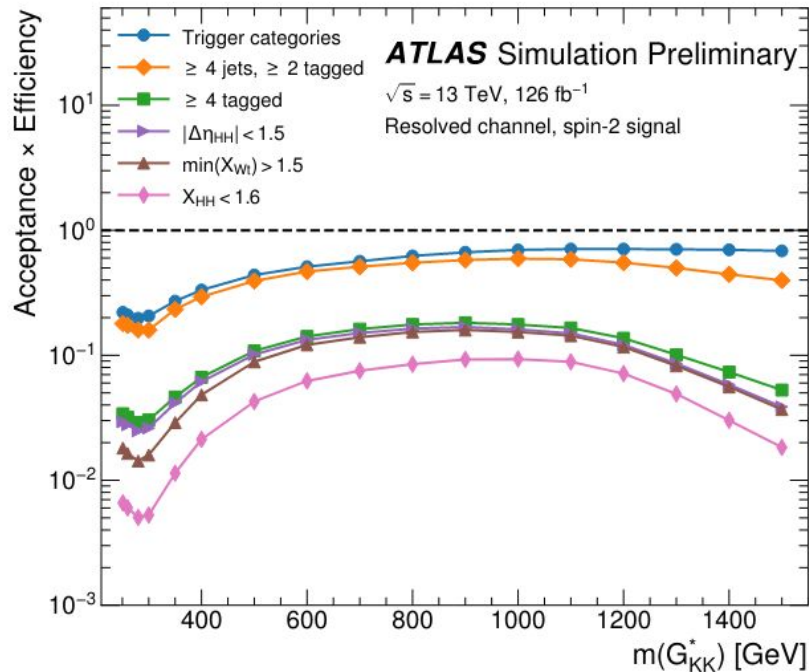
$$X_{HH} = \sqrt{\left(\frac{m(H_1) - 120 \text{ GeV}}{0.1 \times m(H_1)}\right)^2 + \left(\frac{m(H_2) - 110 \text{ GeV}}{0.1 \times m(H_2)}\right)^2}.$$

$$R_{HH}^{\text{VR}} \equiv \sqrt{(m(H_1) - 1.03 \times 120 \text{ GeV})^2 + (m(H_2) - 1.03 \times 110 \text{ GeV})^2} < 30 \text{ GeV}.$$

$$R_{HH}^{\text{CR}} \equiv \sqrt{(m(H_1) - 1.05 \times 120 \text{ GeV})^2 + (m(H_2) - 1.05 \times 110 \text{ GeV})^2} < 45 \text{ GeV}.$$

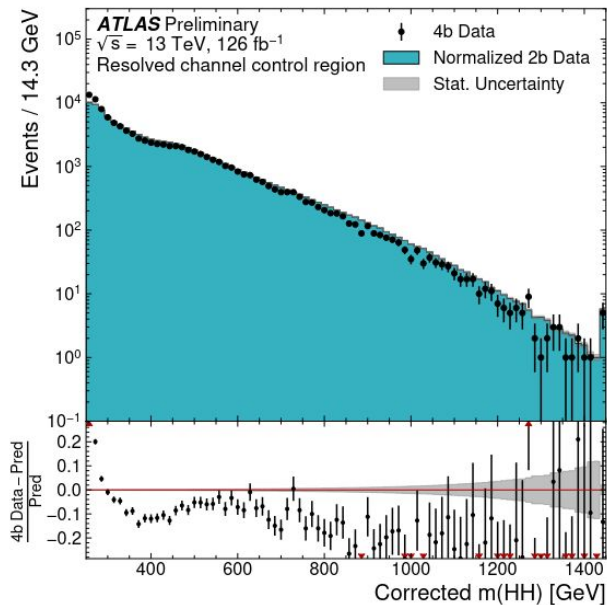


(a)

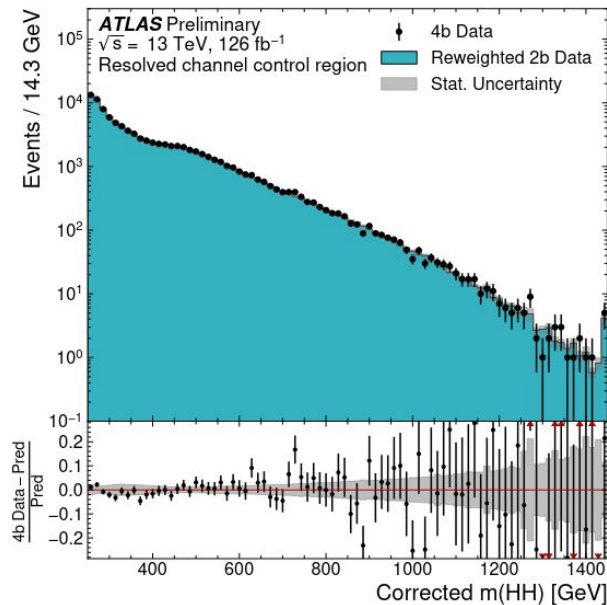


(b)

Figure 3: Cumulative acceptance times efficiency as a function of resonance mass for each event selection step in the resolved channel for (a) the spin-0 and (b) the spin-2 signal models.



(a)



(b)

Figure 4: Corrected $m(HH)$ distributions for the $2b$ control region (teal histogram) and $4b$ control region (dots) in the resolved channel. The statistical uncertainty in the $2b$ control region is represented by the grey band. The error bars on the $4b$ points represent the Poisson uncertainties corresponding to their event yields. The $2b$ data are shown (a) before and (b) after the kinematic reweighting procedure. In both cases the $2b$ distributions are normalized to the $4b$ event yields for a pure shape comparison. The final bin of each distribution includes overflow. The bottom panel shows the difference between the $4b$ and $2b$ distributions, relative to the $2b$ distribution.

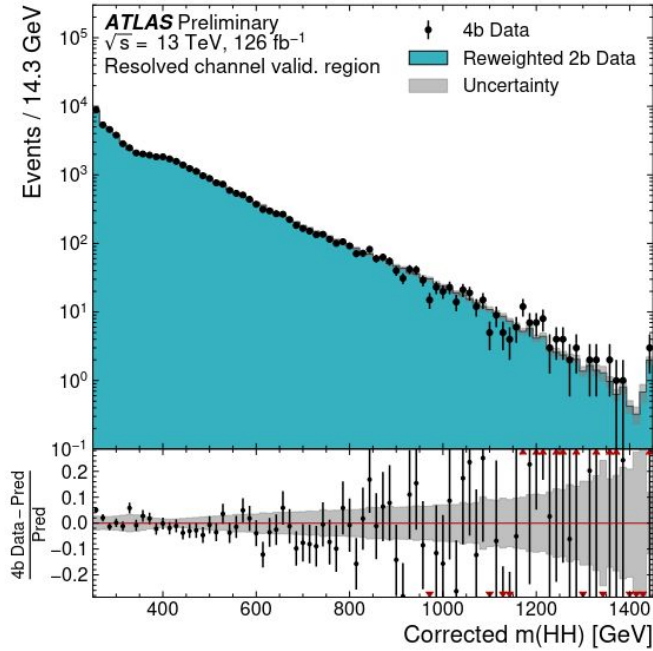


Figure 5: Corrected $m(HH)$ distribution in the resolved $4b$ validation region (dots), compared to the reweighted distribution in $2b$ validation region (teal histogram). The error bars on the $4b$ points represent the Poisson uncertainties corresponding to their event yields. The final bin includes overflow. The background uncertainty (grey band) is computed by adding all individual sources in quadrature. The bottom panel shows the difference between the $4b$ and reweighted $2b$ distributions, relative to the $2b$ distribution.

Table 2: Resolved $4b$ signal region data, estimated background, and signal event yields in corrected $m(HH)$ windows containing roughly 90% of each signal, for representative spin-2 mass hypotheses. The signal is normalized to the overall expected limit on its cross-section; its uncertainties are evaluated by adding all individual components in quadrature. The background yields and uncertainties are evaluated after a background-only fit to the data.

$m(G_{KK}^*)$ [GeV]	Corrected $m(HH)$ range [GeV]	Data	Background model	Spin-2 signal model
260	[250, 393]	26 775	26 650 \pm 130	368 \pm 25
500	[464, 636]	4 655	4 719 \pm 37	138.6 \pm 5.7
800	[707, 950]	795	811 \pm 13	52.1 \pm 1.9
1200	[993, 1279]	146	120.6 \pm 2.8	14.45 \pm 0.67

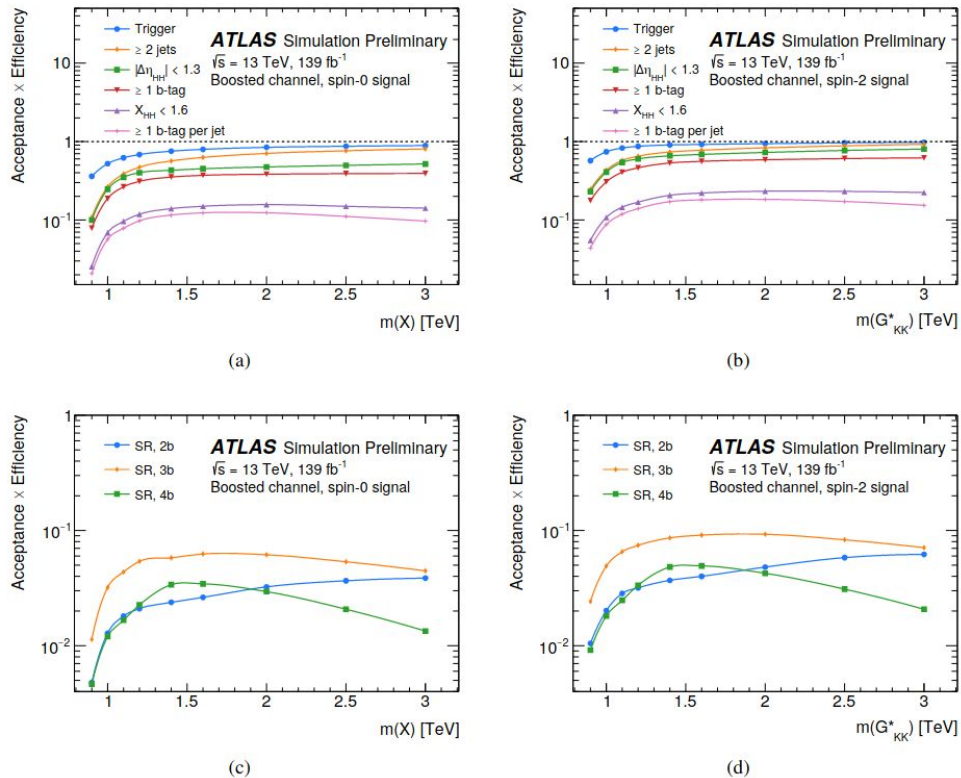


Figure 9: Cumulative signal acceptance times efficiency as a function of the resonance mass for various selection steps in the boosted channel. The steps up to the b -tag categorization are shown for (a) the spin-0 and (b) the spin-2 signal models. The efficiencies of the three b -tag categories are shown for (c) the spin-0 and (d) the spin-2 scenarios; this efficiency is obtained after the other selection steps including the SR definition. The signal efficiency in the $4b$ region has a maximum around 1.5 TeV. Above that value the track jets starts to merge together, and for the highest resonance masses the $3b$ and $2b$ categories become the most efficient.

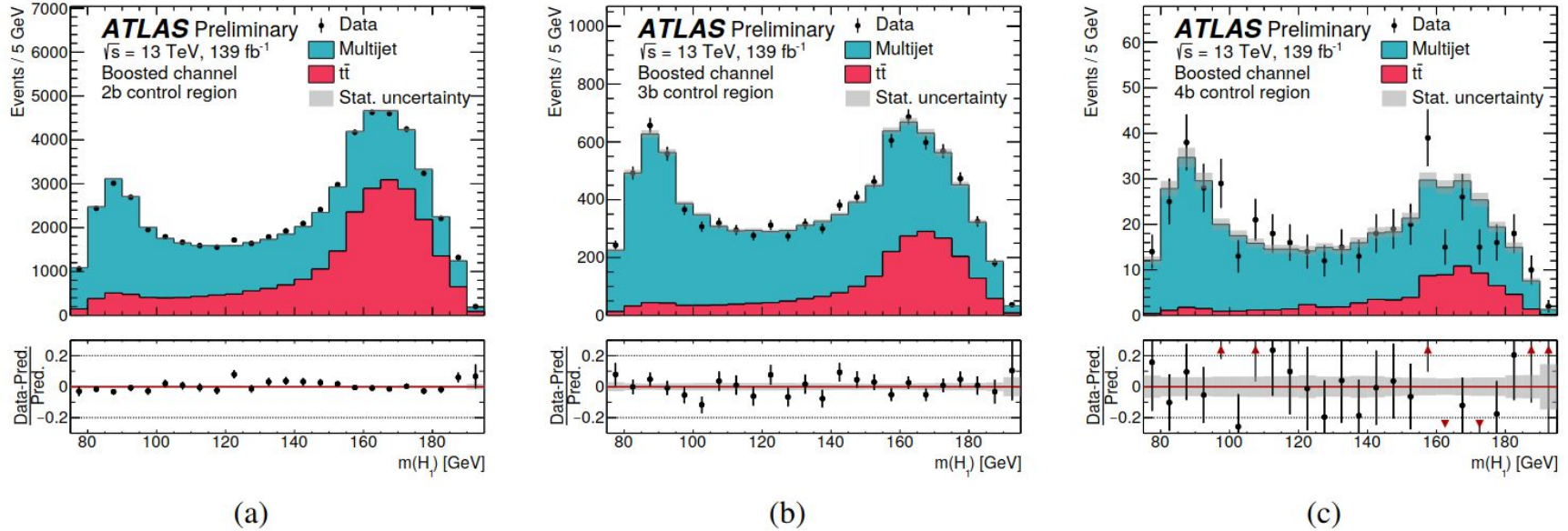


Figure 10: Reconstructed mass distributions of the leading H candidate for the data (dots) and the background model (stacked histograms) in the (a) 2b, (b) 3b and (c) 4b control regions. The error bars on the data points represent the Poisson uncertainties corresponding to their event yields. The statistical uncertainty in the background model is represented by the grey band. This distribution is used to normalize the multijet and $t\bar{t}$ background components. The enhanced event rates at low and high masses are due to the geometry of the CR. The bottom panel shows the difference between the data and the background model, normalized to the background model.